Cell Metabolism

Resource

Cytoarchitectural multi-depot profiling reveals immune-metabolic crosstalk in human colon-associated adipose tissue

Graphical abstract

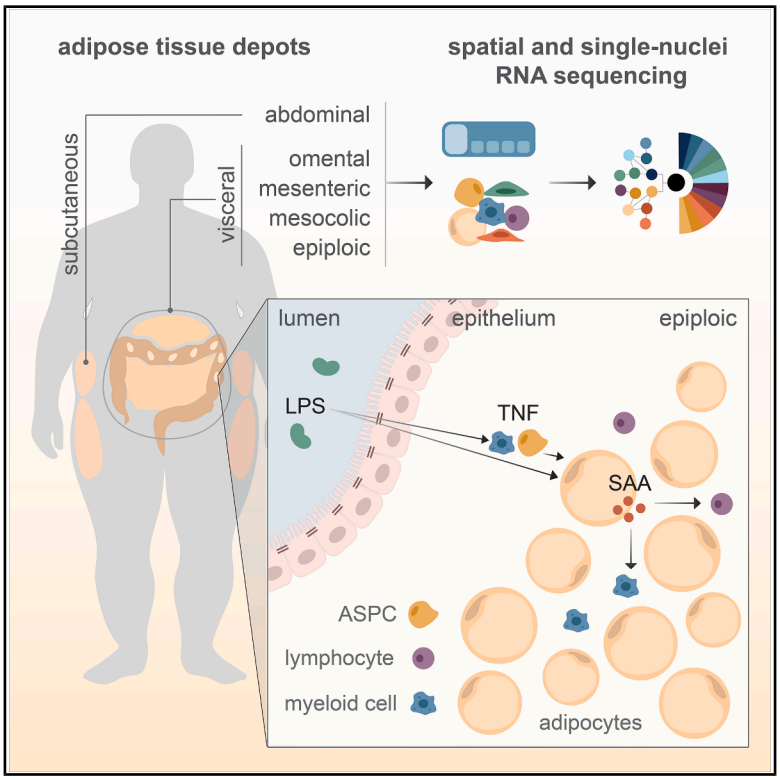

Highlights

- Spatial and single-nucleus mapping reveal diversity across human adipose depots
- Epiploic fat is enriched in immune cells and serum amyloid-positive adipocytes
- Inflammatory cues induce adipocyte serum amyloid A expression
- Visceral fat near the colon exhibits immune-metabolic specialization

Authors

Jutta Jalkanen, Jiawei Zhong, Pamela A. Nono Nankam, ..., Lucas Massier, Mikael Rydén, Niklas Mejhert

Correspondence

lucas.massier@helmholtz-munich.de (L.M.),
mikael.ryden@ki.se (M.R.),
niklas.mejhert@ki.se (N.M.)

In brief

Jalkanen et al. generate spatial and single-nucleus transcriptomic maps of human subcutaneous and visceral white adipose depots, revealing distinct cytoarchitectural and immunologic features. Epiploic adipose tissue is enriched for *SAA1/SAA2*-expressing adipocytes that activate local myeloid cells, highlighting an immune-metabolic specialization in adipose tissue close to the microbiome in the colon.

Jalkanen et al., 2026, Cell Metabolism *38*, 419–433
February 3, 2026
https://doi.org/10.1016/j.cmet.2025.12.008

CellPress

Cell Metabolism

CellPress
OPEN ACCESS

Resource

Cytoarchitectural multi-depot profiling reveals immune-metabolic crosstalk in human colon-associated adipose tissue

Jutta Jalkanen,[1,14] Jiawei Zhong,[1,14] Pamela A. Nono Nankam,[2] Nayanika Bhalla,[3] Merve Elmastas,[1] Jiaxin Luo,[1] Sophie Weinbrenner,[1,2] Scott Frendo-Cumbo,[1] Benedek Pesti,[3] William Gourash,[4] Anita Courcoulas,[4] Zinger Yang Loureiro,[5] Arne Dietrich,[6] Jesper Bäckdahl,[1] Anders Thorell,[7] Marcus Buggert,[8] Joanna Kalucka,[9] Margo P. Emont,[10] Evan D. Rosen,[5,11] Matthias Blüher,[2,12] Peter Kovacs,[12] Patrik L. Ståhl,[3] Lucas Massier,[1,2,14,*] Mikael Rydén,[1,13,14,*] and Niklas Mejhert[1,13,14,15,*]

[1]Department of Medicine (H7), Karolinska Institutet, C2-94, Karolinska University Hospital, Stockholm, Sweden
[2]Helmholtz Institute for Metabolic, Obesity, and Vascular Research (HI-MAG) of the Helmholtz Zentrum München at the University of Leipzig, University Hospital Leipzig, Leipzig, Germany
[3]Science for Life Laboratory, Department of Gene Technology, KTH Royal Institute of Technology, Solna, Sweden
[4]Department of Surgery, University of Pittsburgh Medical Center, Pittsburgh, PA, USA
[5]Division of Endocrinology, Diabetes and Metabolism, Beth Israel Deaconess Medical Center, Boston, MA, USA
[6]Clinic for Visceral, Transplantation, and Thorax and Vascular Surgery, University Hospital Leipzig, Leipzig, Germany
[7]Department of Clinical Sciences, Karolinska Institutet, Danderyd Hospital, Department of Surgery, Ersta Hospital, Stockholm, Sweden
[8]Center for Infectious Medicine, Department of Medicine Huddinge (H7), Karolinska Institutet, Karolinska University Hospital Huddinge, Huddinge, Sweden
[9]Department of Biomedicine, Aarhus University, Aarhus, Denmark
[10]Department of Medicine, Section of Endocrinology, Diabetes, and Metabolism, University of Chicago, Chicago, IL, USA
[11]Harvard Medical School, Boston, MA, USA
[12]Medical Department III – Endocrinology, Nephrology and Rheumatology, University of Leipzig Medical Center, Leipzig, Germany
[13]Steno Diabetes Center Copenhagen, Herlev, Denmark
[14]These authors contributed equally
[15]Lead contact
*Correspondence: lucas.massier@helmholtz-munich.de (L.M.), mikael.ryden@ki.se (M.R.), niklas.mejhert@ki.se (N.M.)
https://doi.org/10.1016/j.cmet.2025.12.008

SUMMARY

While it is well established that the cellular composition of white adipose tissue (WAT) varies between depots, the functional relevance of this heterogeneity remains unclear. By combining spatial and single-nucleus RNA sequencing, we provide a comprehensive map of subcutaneous and visceral (omental, mesenteric, mesocolic, and epiploic) WAT in both men and women. Our analyses reveal shared features, such as the spatial organization of adipogenesis, alongside depot-specific characteristics, including distinct cell-type enrichments and unique cell-cell communication routes. Epiploic WAT stands out by harboring high proportions of serum amyloid A expressing fat cells (encoded by *SAA1/SAA2*) and several leukocyte populations. Through mechanistic studies, we demonstrate that adipocyte *SAA1/SAA2* expression is induced by inflammatory signals, including lipopolysaccharide, and that SAA1 activates immune responses in adipose-resident myeloid cells. Collectively, our findings suggest that visceral WAT exhibits distinct cytoarchitectural properties, with those located near the colon adapting by developing specialized adipocytes and immune cell populations.

INTRODUCTION

Multiple studies have revealed substantial cellular heterogeneity within white adipose tissue (WAT), encompassing distinct populations of adipocytes, leukocytes, vascular cells, and adipose stromal and progenitor cells (ASPCs), all of which collectively regulate tissue function.[1] Out of the visceral depots, omental fat has been extensively compared with subcutaneous WAT.[2–4] However, far less is known about the cellular composition and structural organization of other visceral regions, including the mesenteric, mesocolic, mesorectal, and epiploic depots, which remain underexplored in human studies. These depots, positioned along the gastrointestinal tract, are thought to provide mechanical protection, metabolic support, and immune surveillance in response to gut-derived signals.[5,6] Among the few studies that have investigated these sites, Krieg et al.

identified multiple differences across visceral WAT depots, where links to insulin resistance were most prominent in epiploic WAT.[7] Others have reported that mesenteric fat harbors smaller adipocytes and a higher proportion of B cells, compared with the mesocolic region.[5] However, these studies did not employ high-resolution -omics technologies, leaving key aspects of visceral WAT heterogeneity unexplored.

Here, we comprehensively profiled abdominal subcutaneous and four visceral depots from eight men and women using single-nucleus RNA sequencing (snRNA-seq) and spatial transcriptomics (STx). Through integrative analyses, using existing and in-house-developed tools, we uncovered unexpected structural organization of all five depots and identified region-specific cellular features, including distinct cell-cell communication routes. Mechanistically, we observed intricate interactions between adipocytes and myeloid cells, which were particularly pronounced in epiploic WAT. These findings highlight the complex cellular architecture and functional diversity within different adipose depots.

RESULTS

Adipose depots display qualitative and quantitative differences in cell composition

To define the cellular landscape of WAT, we profiled five different adipose depots. More specifically, we performed STx and snRNA-seq on biopsies from the abdominal subcutaneous, greater omental, mesenteric (close to the duodenum/jejunum), and mesocolic regions (close to the transverse colon) and from epiploic appendices (on the transverse colon) (Figure 1A). These sites were selected because they are anatomically distinct and accessible during intra-abdominal surgery. In total, eight donors (n = 4 men and n = 4 women) undergoing gastric bypass surgery for severe obesity were included in the study. Selected clinical variables are displayed in Figure 1B, with a full clinical description in Table S1.

After quality control, including ambient RNA removal and doublet exclusion, we obtained transcriptional data from a total of 61,560 spots (from 36 STx samples) and 255,273 nuclei (from 34 snRNA-seq samples), which were evenly distributed across depots and donors (Figures 1B and S1A). For the STx data, we applied *SpotClean*[8] to reduce the effects of diffused transcripts. Next, we integrated the STx and snRNA-seq results across donors and depots using *Harmony*[9] and *scVI*,[10] respectively, as these methods perform well on data obtained using the two platforms.[11,12] As presented in Figures 1C and S1B, manual annotation of the major snRNA-seq clusters revealed six classes encompassing (1) ASPCs, (2) mesothelial cells, (3) vascular cells, (4) immune cells (myeloid and lymphoid), (5) adipocytes, and (6) Schwann cells (a small group of glial cells). To determine variations in cell class abundance across depots, we quantified their proportions by region. Consistent with previous studies,[2,13] our data showed that ASPCs constituted 20%–30%, mesothelial cells 10%–25% (albeit not detected in subcutaneous WAT), vascular cells 5%–15%, immune cells 30%–50%, adipocytes 20%–25%, and Schwann cells constituted <1% of the total cell population (Figures 1D and S1C). The latter was predominantly detected in one donor and was therefore not further investigated. Because all donors in our study were individuals living with severe obesity, we compared marker gene expression with the snRNA-seq dataset from Emont et al.[2] Adipocytes from our cohort clustered with those from individuals with obesity, while other cell classes showed no body mass index (BMI)-related separation (Figure S1D). Thus, our data are representative of high-BMI adipose tissue and show that the examined depots display qualitative and quantitative differences in cell composition.

Stromal-vascular heterogeneity distinguishes adipose depots

We next re-clustered the data and annotated the resulting identities to obtain a more detailed view of the composition of each cell class. Except for adipocytes, which are difficult to reproducibly subdivide using snRNA-seq,[13] all stromal-vascular classes contained cell signatures displaying significant differences comparing depots (Figures 2 and S2A–S2J; Table S2). As expected, subcutaneous WAT lacked mesothelial cells but was enriched in apolipoprotein D (*APOD*)-expressing ASPCs, vascular endothelial cells, and specific immune cell populations, including lipid-associated macrophages and mast cells. The mesenteric and mesocolic depots exhibited similar cellular compositions, whereas omental and epiploic WAT displayed distinct differences. Notably, the omental depot was enriched in a unique mesothelial cell subtype, as well as late-committed ASPCs (committed preadipocytes [CPAs]) and *IGFBP2*$^{+}$ ASPCs. The latter observation aligns with previous data from Ferrero et al.[14] In contrast, the epiploic depot displayed a marked enrichment of tissue-resident and recruited myeloid and lymphoid cells, including type 2 conventional dendritic and T helper 17 cells. Altogether, our results show that the studied depots differ in stromal-vascular composition, with subcutaneous, omental, and epiploic WAT displaying distinct profiles.

Adipo^{SAA} is enriched in epiploic adipose tissue

For adipocyte subtype classification, we focused on the STx data. By separately re-clustering the spots dominated by adipocyte signatures, our analysis identified three fat cell identities, which displayed striking similarities to Adipo^{LEP}, Adipo^{PLIN}, and Adipo^{SAA}, described by Bäckdahl et al.[12] (Figures 3A and 3B). Specifically, Adipo^{LEP} was marked by genes encoding leptin (*LEP*), cold shock domain containing E1 (*CSDE1*), and tensin 1 (*TNS1*); Adipo^{PLIN} was enriched in perilipin 1 and 4 (*PLIN1* and *PLIN4*, respectively) and adiponectin (*ADIPOQ*); while Adipo^{SAA} showed high expression of genes linked to retinol transport and metabolism, including serum amyloid alpha 1 and 2 (*SAA1* and *SAA2*) and carboxylesterase 1 (*CES1*). Analyses of published bulk transcriptomics data[15–18] and qPCR of fractionated WAT showed that these markers were primarily expressed in adipocytes rather than other adipose-resident cell types, suggesting that the observed heterogeneity is not due to cell-type mixtures within or near the corresponding *Visium* spot (Figures S3A–S3D). We next examined if these fat cell identities differed in terms of tissue abundance. Our results show that while Adipo^{LEP} and Adipo^{PLIN} were more evenly distributed across depots, Adipo^{SAA} displayed enrichment in epiploic WAT (Figure 3C). To validate these findings, we assessed Adipo^{SAA} marker genes in our snRNA-seq results and in previously published bulk transcriptomic and proteomic data.[7] All three datasets

CellPress
OPEN ACCESS

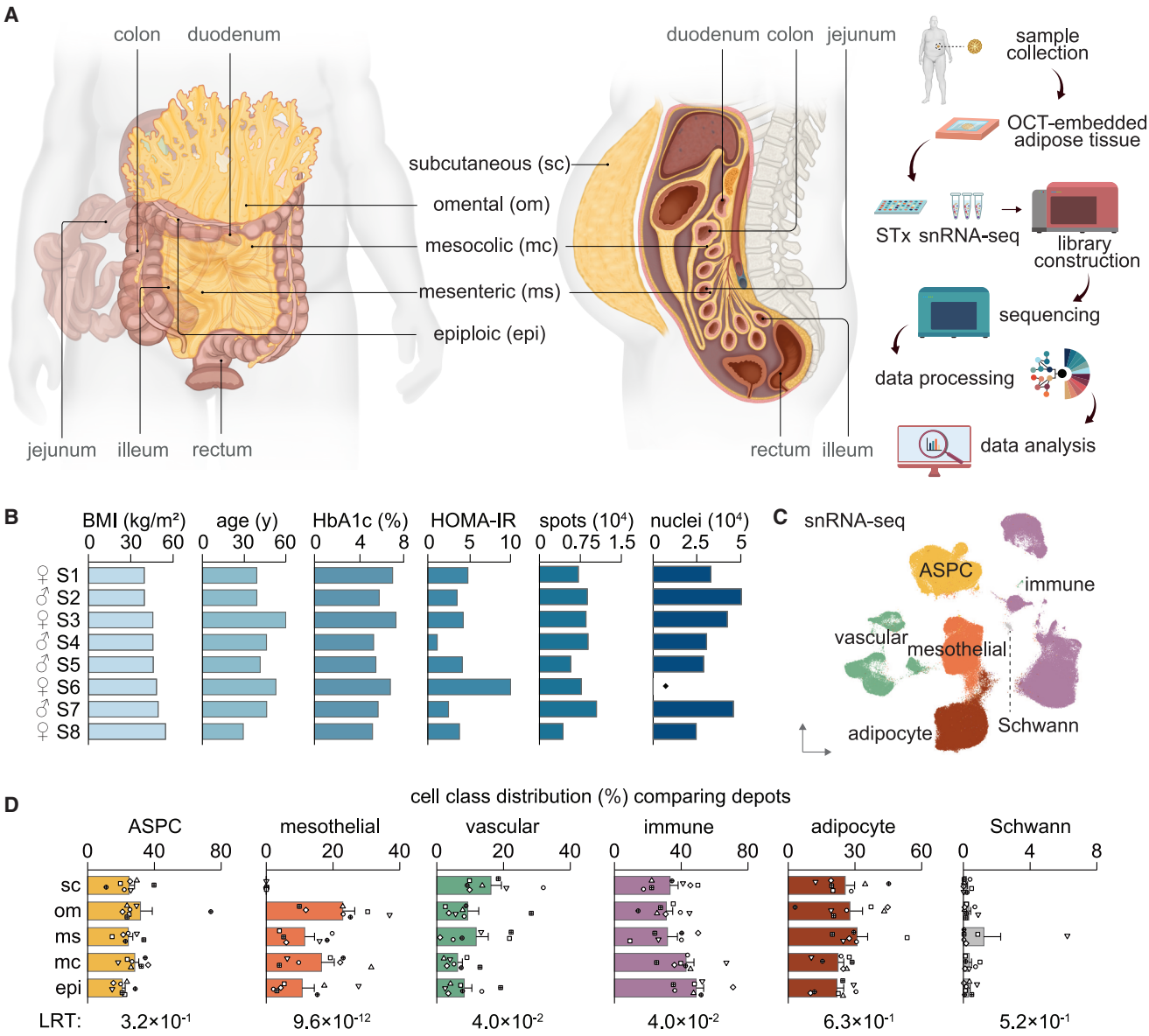

Figure 1. Adipose tissue depots show variations in cellular composition

(A) Overview of the studied WAT depots, indicating their anatomical localization and the analysis pipeline, which integrates data from snRNA-seq and STx.

(B) Selected clinical data and the number of spots and nuclei per individual included in the study. Sex is denoted by symbols. As indicated by the asterisk, no nuclei were isolated for participant S6.

(C) Uniform manifold approximation and projection displaying the six main cell classes identified in the snRNA-seq data.

(D) Cell class distribution per depot and subject (n = 7, indicated by subject-specific symbols), expressed as a percentage of the total cell population (excluding mesothelial cells) for all non-mesothelial cell types. For mesothelial cells only, the results are provided as a percentage of the total cellular pool. p values from likelihood ratio tests (LRTs) comparing depots and error bars (standard error of the mean) are displayed.

ASPC, adipose stromal and progenitor cell; BMI, body mass index; HOMA-IR, homeostasis model assessment insulin resistance; y, years.

displayed high expression levels of Adipo^{SAA} markers in the epiploic depot, thereby corroborating the STx results (Figure 3D). To confirm this result in samples collected and processed independently, we generated snRNA-seq data from a validation cohort comprising four subjects (two men and two women), where adipose tissue was available from the abdominal subcutaneous, omental, and epiploic depots (n = 12 samples). Comparisons of these data with the snRNA-seq results generated herein and by others[2] revealed that *SAA1*, *SAA2*, and *CES1* were predominantly expressed in a subpopulation of adipocytes and enriched in the epiploic depot (Figures 3D, S3E, and S3F). We also stained tissue sections with an antibody targeting CES1, choosing this protein as it, in contrast to SAA1 and SAA2, is not secreted. Compared with the other WAT regions, we observed the highest CES1 staining intensity in epiploic and mesocolic fat, two depots that are positioned close to the colon (Figures 3E and S3G). The

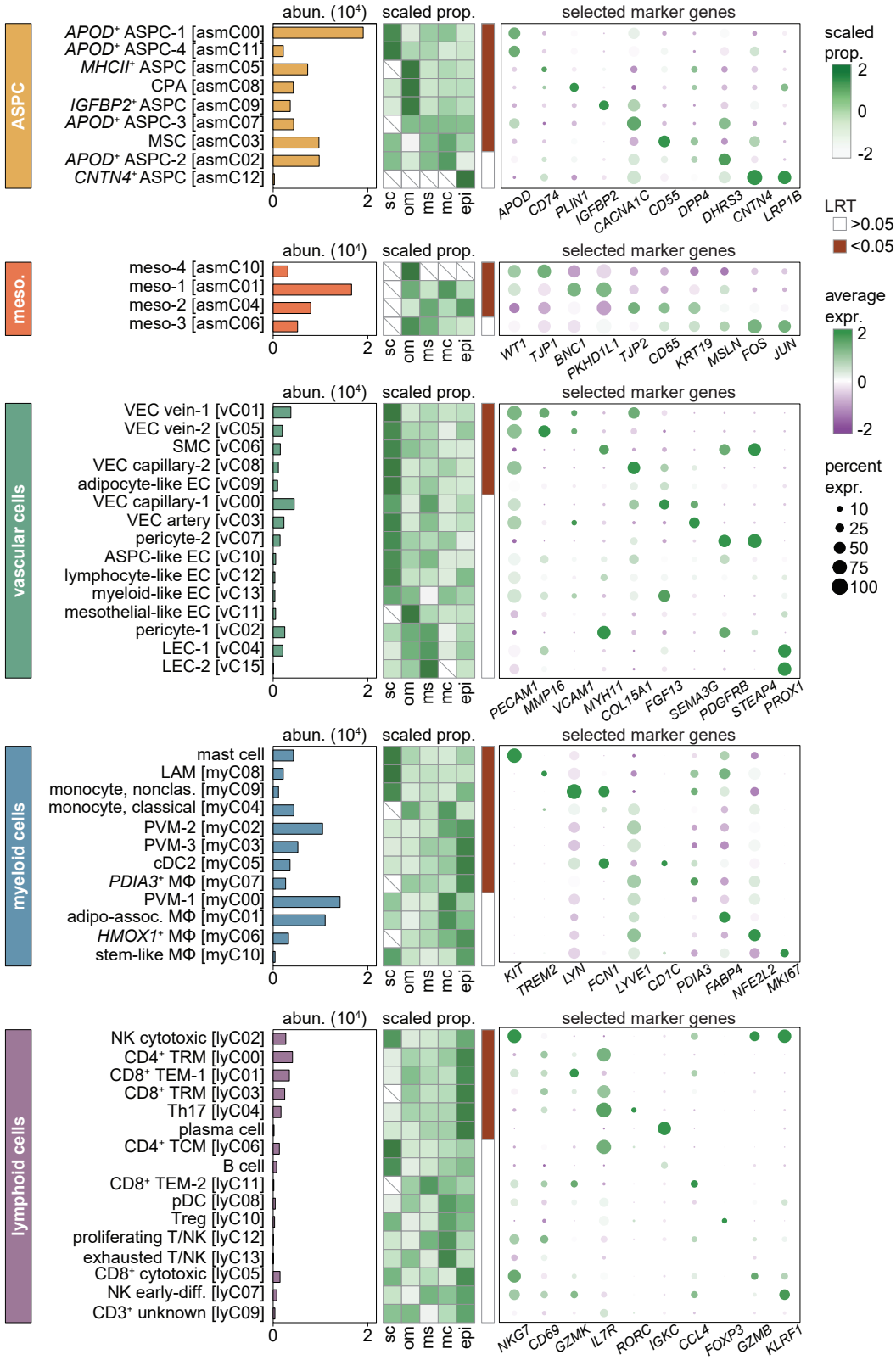

Figure 2. The stromal-vascular cellular landscape varies between WAT depots

Cell name (identity), abundance (abun.), scaled proportion (prop.), and scaled (z-transformation) average expression (expr.) of selected marker genes for high-resolution cell identities across depots. Results are displayed by cell class with significantly enriched ($p < 0.05$ using LRT) identities indicated.

(legend continued on next page)

CellPress
OPEN ACCESS

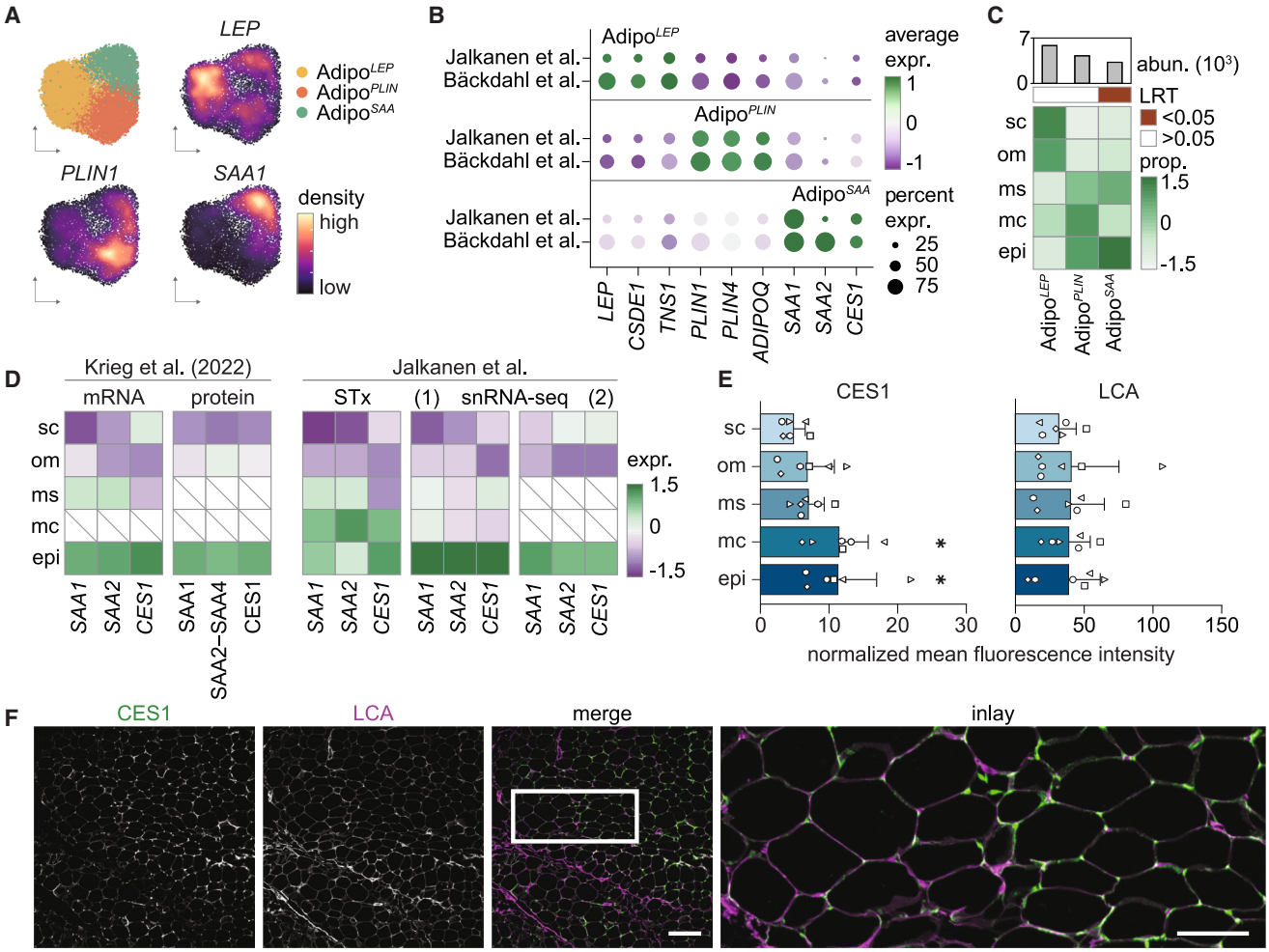

Figure 3. STx reveals epiploic enrichment of Adipo^{SAA}

(A) Uniform manifold approximation and projection displaying adipocyte identities and expression densities for main marker genes in the STx data.

(B) Dot plots displaying the scaled average expression (expr.) profiles of the top three marker genes for each adipocyte identity in the present work and a previous study.[12]

(C) Abundance (abun.) and depot enrichments (scaled proportions, prop.) for the three main adipocyte identities. Significant enrichments ($p < 0.05$ using likelihood ratio test, LRT) are indicated.

(D) Heatmaps displaying expressional enrichments of Adipo^{SAA} markers across depots. Results are shown as scaled average expression for bulk transcriptomics and proteomics from Krieg et al.,[7] as well as STx and snRNA-seq in the main (1) and validation (2) cohorts.

(E) Quantification of CES1 and lectin (LCA) normalized mean fluorescence intensity based on tissue sections from six individuals imaged using confocal microscopy. Asterisks denote statistically significant differences (*$p < 0.05$) comparing depots using one-way repeated measures ANOVA and Tukey's multiple comparisons test. Error bars are standard error of the mean.

(F) Representative image of epiploic WAT stained with LCA and an antibody directed against CES1. Scale bars, 200 μm (merge) and 100 μm (inlay).

epi, epiploic; mc, mesocolic; ms, mesenteric; om, omental; sc, subcutaneous.

CES1 signal was unevenly distributed in contrast to the relatively even lectin signal, suggesting cellular heterogeneity, which is expected for a subtype marker protein (Figure 3F). Overall, our findings demonstrate that STx reproducibly identifies adipocyte clusters where Adipo^{SAA} is particularly enriched in epiploic WAT.

Adipose tissue is organized in distinct spatial niches

To provide spatial context to our results, we deconvolved the STx data with annotated snRNA-seq matrices using *cell2location*, which assigns probabilistic cell-type compositions to each spot.[19] Building on these estimates, we developed spatial

ASPC, adipose stromal and progenitor cell; cDC2, type 2 conventional dendritic cell; CPA, committed preadipocyte; epi, epiploic; LAM, lipid-associated macrophage; LEC, lymphatic endothelial cell; Mϕ, macrophage; mc, mesocolic; meso, mesothelial cells; ms, mesenteric; MSC, mesenchymal stem cell; NK, natural killer cell; om, omental; pDC, plasmacytoid dendritic cell; PVM, perivascular macrophage; sc, subcutaneous; SMC, smooth muscle cell; Th17, T helper 17 cell; TCM, central memory T cell; TEM, effector memory T cell; Treg, regulatory T cell; TRM, tissue-resident memory T cell; VEC, vascular endothelial cell.

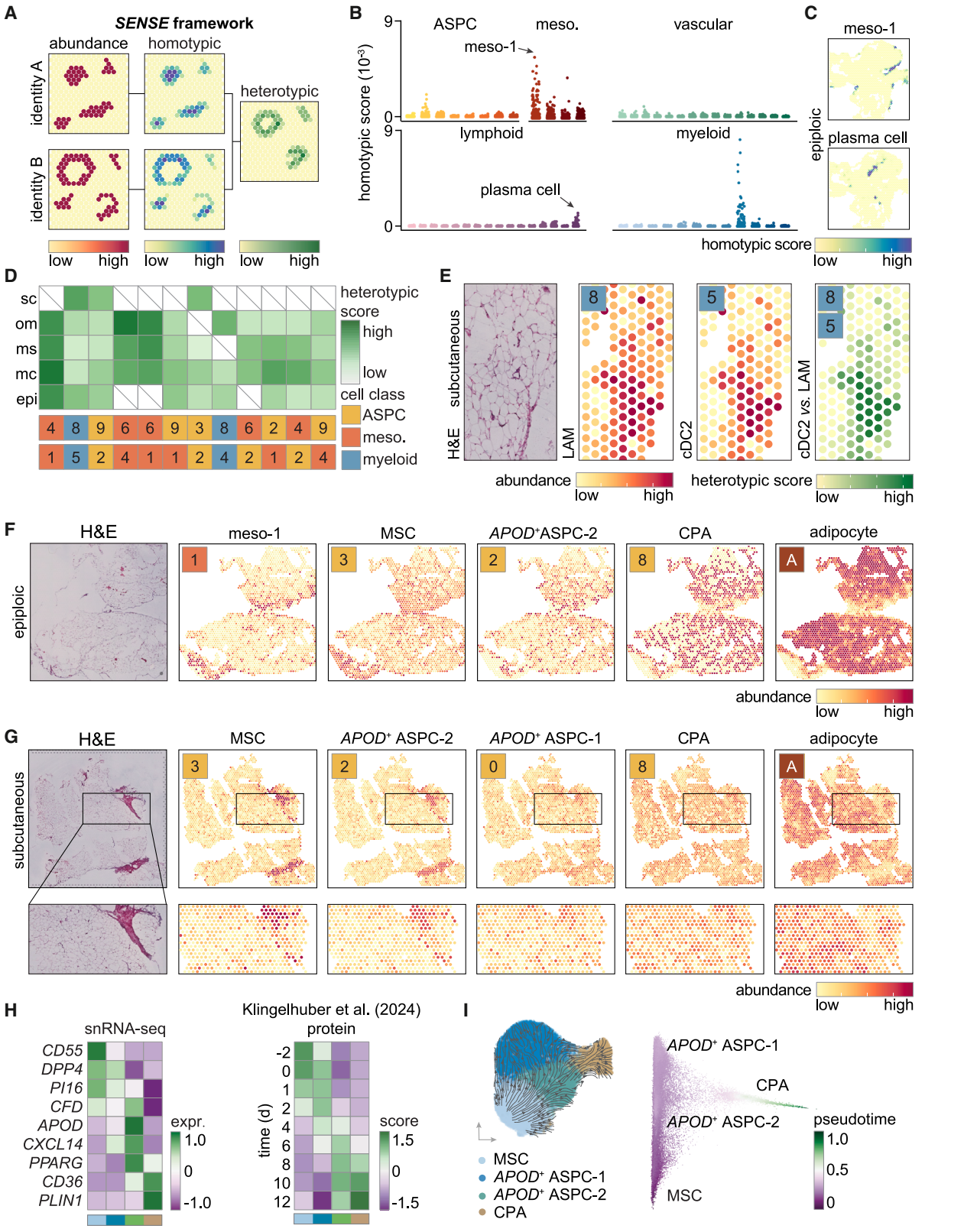

Figure 4. Distinct spatial niches define adipose tissue organization

(A) Overview of the homotypic and heterotypic score calculations. The *SENSE* framework quantifies homotypic (self-clustering preference) and heterotypic (preferential co-localization between identities) scores.

(legend continued on next page)

neighborhood enrichment analysis and evaluation (*SENSE*), a framework that quantifies whether cell types preferentially cluster with themselves (homotypic distribution) or with other cell types (heterotypic distribution) (Figure 4A). As detailed in the STAR Methods section, these scores were calculated by weighing each cell type's proportion at a given spot according to the proportion of the neighboring spots. Expected values were generated by randomizing spatial coordinates across 50 iterations to correct for differences in cell-type abundance. The final enrichment scores were standardized by subtracting the mean expected value and dividing by its standard deviation. Specific mesothelial and myeloid cells, as well as plasma cells, exhibited high homotypic scores, whereas most other cell types were more broadly dispersed across the tissue (Figures 4B and 4C). We validated the mesothelial cell findings using an antibody targeting keratin 19 (Figures S4A and S4B). For heterotypic localization, our analysis identified spatially defined domains that were either shared across multiple WAT regions or unique to a single depot (Figures 4D and S4C). Among the shared domains, we observed two major patterns: (1) specific myeloid identities (classical monocytes, type 2 conventional dendritic cells, and lipid-associated macrophages) were clustered together, and (2) mesothelial cells were positioned near ASPCs (Figures 4D, 4E, and S4D). Further analysis revealed that ASPCs were spatially organized into distinct layers, with $CD55^{+}$ mesenchymal stem cells positioned near the mesothelium in visceral fat and within connective tissue-rich, vessel-free regions in subcutaneous WAT (Figures 4F, 4G, and S4E). For the latter, our findings align with mouse studies showing that these cells are excluded from the perivascular compartment and instead reside in the elastin- and fiber-rich reticular interstitium.[20–22] In contrast, CPAs were found closer to mature adipocytes, while *APOD*$^{+}$ ASPCs occupied an intermediate position between these two layers (Figures 4F and 4G). To determine whether this arrangement reflected an adipogenic trajectory, we deconvolved bulk transcriptomic and proteomic data encompassing various stages of human adipocyte *de novo* formation.[16,18,23] As displayed in Figure 4H, this analysis demonstrated that the layered ASPC populations expressed marker genes encoding proteins enriched at specific time points of adipogenesis, going from stem cells to intermediate and more committed stages. Furthermore, pseudo-time analysis of these identities by *CellRank2*[24] also aligned them along the adipogenic trajectory in all five depots (Figures 4I and S4F). Collectively, these findings reveal an unrecognized structural WAT organization with distinct layered cellular arrangements originating from adipogenic niches near the visceral mesothelium or the subcutaneous reticular interstitium.

The epiploic depot displays inflammatory and tissue remodeling signals

Having established the cell proportions and spatial organization of these depots, we next inferred cell-cell communication using *CellChat*.[25] Our analysis revealed that epiploic WAT exhibited higher numbers of interactions and stronger predicted signaling activity, compared with the other depots (Figure 5A). To investigate the drivers of these differences, we analyzed incoming and outgoing signaling strengths for each cell class. While all of them contributed to the elevated communication observed in epiploic WAT, specific patterns emerged; mesothelial cells, lymphoid cells, and adipocytes primarily acted as signal senders, whereas vascular and myeloid cells predominantly received signals. In contrast, ASPCs maintained a balanced role, sending and receiving similar numbers of signals (Figure 5B). Further analysis of ligand-receptor interactions enriched in the epiploic region identified pathways associated with extracellular matrix remodeling, cell migration, and inflammation (Figure 5C; Table S3). Pseudobulk comparisons of our snRNA-seq results confirmed an enrichment of these processes in epiploic vs. subcutaneous WAT (Figure 5D; Table S4). We obtained similar data when repeating the analyses in the validation cohort (Figures S5A–S5D). Together with our findings presented above, these results highlight that epiploic fat harbors distinct populations of fat cells and leukocytes, where adipocytes and lymphoid cells primarily drive signaling, while myeloid cells predominantly act as receivers.

LPS and TNF-α induce *SAA1* and *SAA2* expression in adipocytes

Given the enrichment of $Adipo^{SAA}$ and immune cells in epiploic WAT, we next sought to determine whether these cell types engage in direct or indirect signaling interactions that might shape the depot's cellular landscape. SAA proteins have been suggested to promote immune responses via binding to LDL receptor-related protein 1 (LRP1),[26] Toll-like receptor 2 (TLR2),[27] and formyl peptide receptor 2 (FPR2).[28,29] To explore these signaling pathways, we compared receptor expression and estimated cell-cell communication across depots. While all three receptors were expressed in each region, epiploic WAT exhibited stronger adipocyte-to-ASPC and adipocyte-to-myeloid cell SAA signaling, compared with the subcutaneous depot in both snRNA-seq cohorts (Figures 6A, S6A, and S6B).

We next asked whether the signaling environment of epiploic WAT might promote *SAA1* and *SAA2* expression. While the mRNA levels of inflammatory markers were similar comparing depots, pseudobulk comparisons of epiploic vs. subcutaneous WAT revealed enrichment of genes encoding lipopolysaccharide (LPS)-binding proteins and receptors (LBP, CD14, and TLR4),

(B and C) Homotypic scores for the indicated cell identities across all depots (B) and examples of cell types with high scores (C).
(D) Heatmap displaying heterotypic scores across depots for the indicated cell identity pairs. For the latter, colors and numbers refer to the nomenclature presented in Figure 2.
(E) Representative example of identities displaying high heterotypic scores in subcutaneous fat.
(F) Distribution of mesothelial cells (meso-1), mesenchymal stem cells (MSCs), *APOD*$^{+}$ ASPC-2, CPAs, and adipocytes in epiploic fat.
(G) Same as in (F), but for the subcutaneous region. Note the lack of mesothelial cells and the presence of *APOD*$^{+}$ ASPC-1.
(H) Scaled average expression (expr.) of marker genes in snRNA-seq (left) or protein deconvolution scores from Klingelhuber et al.[23] across adipogenesis (right) for the indicated cell identities.
(I) Pseudo-time analyses of the indicated cell identities across all depots.
For (E)–(G), the box in the top left corner refers to the cell class identity presented in (D). cDC2, type 2 conventional dendritic cells; epi, epiploic; H&E, hematoxylin and eosin; LAM, lipid-associated macrophage; mc, mesocolic, meso, mesothelial cells; ms, mesenteric; om, omental; sc, subcutaneous.

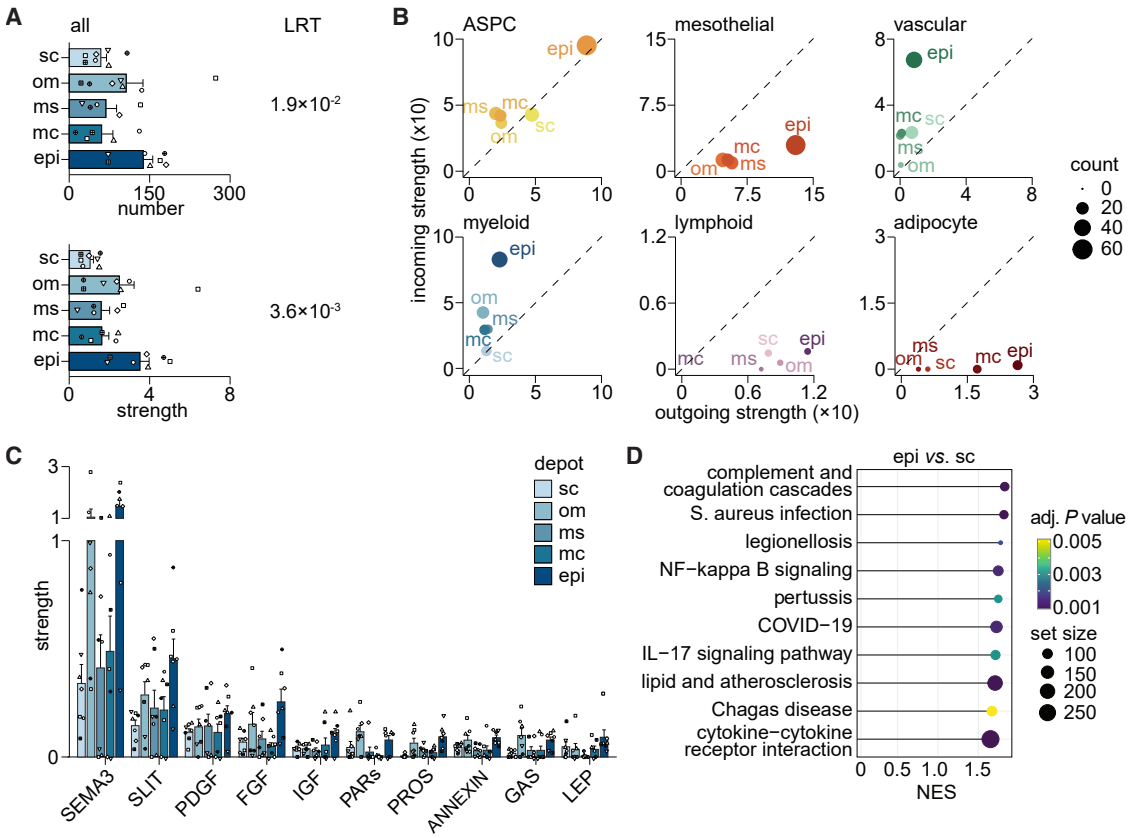

Figure 5. The epiploic depot displays pronounced inflammatory signals

(A) Number (upper) and strength (lower) of predicted cell-cell communication displayed by depot and subject (n = 7, indicated by subject-specific symbols). p values are from likelihood ratio tests (LRTs) and error bars represent standard error of the mean.

(B) Incoming and outgoing strengths displayed per cell class and depot.

(C) Top 10 cell-cell communication pathways displayed per depot using the same color code and symbols as in (A). Error bars represent standard error of the mean.

(D) Top 10 Kyoto Encyclopedia of Genes and Genomes (KEGG) pathways identified through comparisons of epiploic vs. subcutaneous WAT.

ASPC, adipose stromal and progenitor cell; epi, epiploic; mc, mesocolic; ms, mesenteric; NES, normalized enrichment score; om, omental; sc, subcutaneous.

together with downstream signaling proteins in the nuclear factor kappa B (NF-κB), mitogen-activated protein kinase, and signal transducer and activator of transcription (STAT) pathways (Figures 6B, S6C, and S6D). Our observations led us to hypothesize that activators of these signaling axes may stimulate *SAA1* and *SAA2* expression in human adipocytes. Indeed, LPS and tumor necrosis factor alpha (TNF-α) strongly upregulated *SAA1* and *SAA2* mRNA levels, while interleukin-1β (IL-1β) and IL-6 alone or in combination elicited more modest effects (Figure 6C). These results together with the anatomical proximity of the epiploic WAT to the gut microbiome, a major source of endotoxin, suggest a potential role for LPS-driven signaling in this depot.[30–33] Treating human adipocytes with LPS induced a concentration-dependent increase in *SAA1* and *SAA2* expression, which was confirmed at the protein level and sustained for several hours (Figures 6D, 6E, and S6E). This response was adipocyte specific, as ASPCs, endothelial cells, THP1 macrophages, and CD45^{+} adipose cells did not upregulate *SAA1* and *SAA2* despite induction of known LPS-responsive genes such as C-C motif chemokine ligand 2 and C-X-C motif chemokine ligand 8 (Figures 6D, S6F, and S6G). Our results align with previous data demonstrating that LPS induces SAA production primarily in adipocytes.[34] To further investigate the basis of this cellular specificity, we analyzed paired snRNA-seq and methyl-3C data from Chen et al.[35] In line with our own datasets, *SAA1* and *SAA2* were enriched in adipocytes, compared with other adipose-resident cells (Figure S6H). This was accompanied by *SAA1* and *SAA2* promoter hypomethylation in adipocytes, while gene body methylation remained unchanged (Figure S6I). These findings point to promoter methylation as a potential regulatory layer of *SAA1* and *SAA2* transcription, consistent with reports linking reversible demethylation of the *SAA1* promoter to expression in hepatic and non-immune cells.[36]

To delineate the signaling pathways underlying the induction of *SAA1* and *SAA2* in adipocytes, we examined phosphorylation events following LPS stimulation. Based on our pseudobulk analysis presented in Figures 6B and S6D, we focused on NF-κB and STAT3, two transcription factors known to regulate early- and late-phase responses downstream of TLR4 activation.[37–41] Motifs for these regulators are present in the hypomethylated

CellPress
OPEN ACCESS

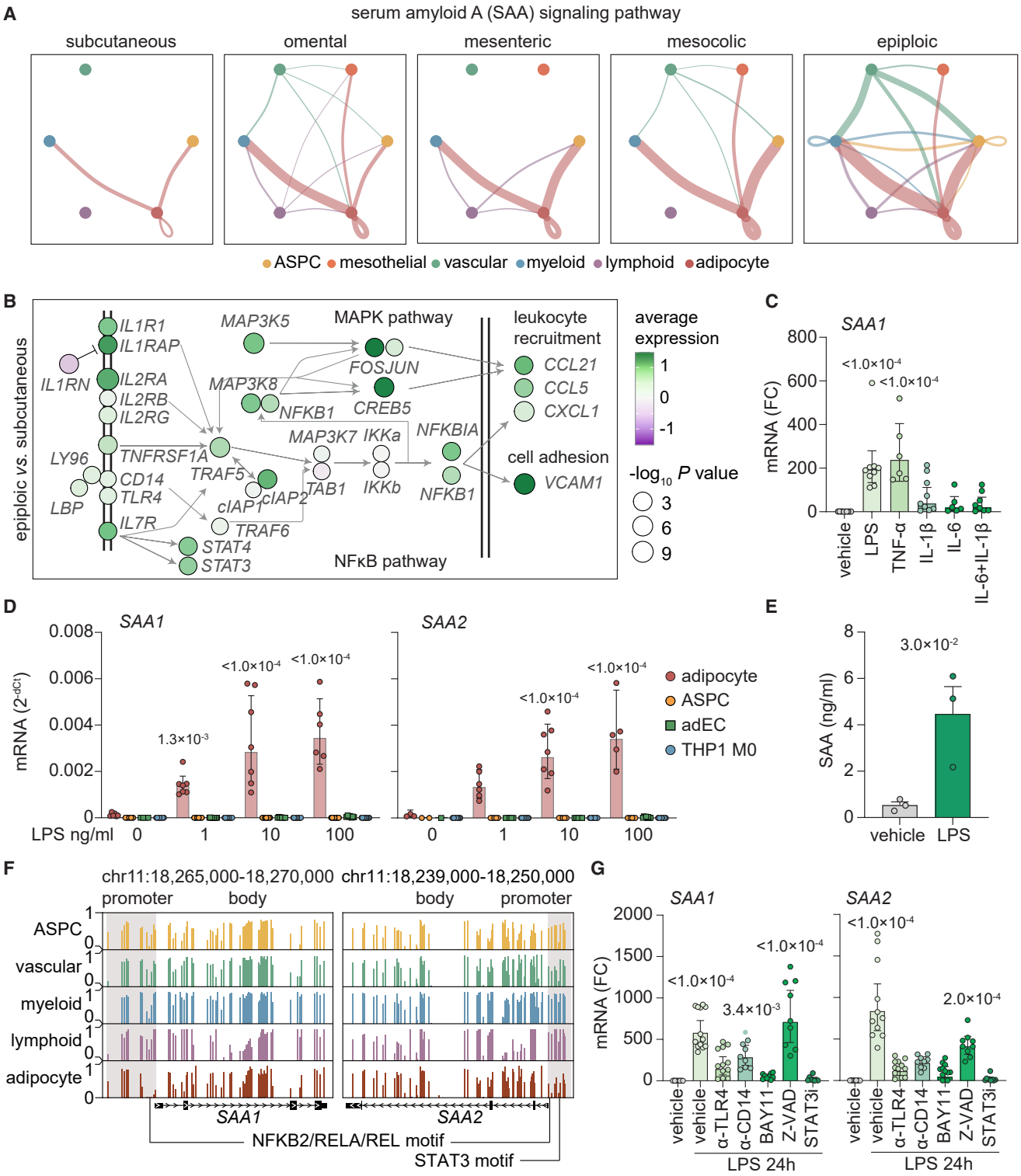

Figure 6. Inflammatory cues drive *SAA1*/*SAA2* expression in adipocytes

(A) Cell-cell communication analysis of SAA signaling pathway for the indicated depots and cells. Line colors and widths represent the sending cell and the strength of the signal, respectively.

(B) Pseudobulk comparison of differentially expressed genes in epiploic vs. subcutaneous depots, highlighting the indicated signaling pathways.

(C) Expression of *SAA1* mRNA upon stimulation with LPS (10 ng/mL), TNF-α (2.5 ng/mL), IL-1β (10 ng/mL), or IL-6 (10 ng/mL) for 24 h. Data are presented as fold change (FC) over vehicle. Significant (<0.05) *p* values compared with the vehicle from one-way ANOVA are shown.

(legend continued on next page)

SAA promoter regions (Figure 6F), and we observed rapid phosphorylation of NF-κB, while STAT3 phosphorylation increased progressively over a 24-h period following LPS stimulation (Figure S6J). Consistent with this, inhibiting these pathways using BAY 11-7082 (NF-κB inhibitor), STAT3 inhibitor VII (STAT3 inhibitor), or antibodies directed against TLR4 and CD14, attenuated LPS-induced *SAA1* and *SAA2* expression (Figure 6G). In contrast, treatment with Z-VAD-FMK (pan-caspase inhibitor) had no effect, indicating that caspase-dependent mechanisms were not involved (Figure 6G). Altogether, our findings suggest that *SAA1* and *SAA2* mRNA levels in adipocytes are regulated by inflammatory cues, with TNF-α and LPS serving as key inducers through NF-κB- and STAT3-dependent pathways.

Myeloid cells respond to SAA1 by inducing pro-inflammatory pathways

Finally, we set out to validate the predicted cellular targets of SAA1 identified through our ligand-receptor analyses. To this end, we isolated the stromal-vascular fraction from subcutaneous WAT and incubated the cells with recombinant human SAA1 for 6 h, using LPS as a comparator. We found that both ligands regulated pathways related to inflammation, including cytokine-cytokine receptor interactions and JAK-STAT signaling (Figure 7A; Tables S5 and S6). However, the gene sets driving these enrichments were only partly overlapping (Figure 7B). This divergence was further reflected by the presence of distinct signatures where SAA1 preferentially induced immune-metabolic programs including TLR signaling and carbohydrate and amino acid metabolism, whereas LPS affected oxidative phosphorylation, extracellular matrix, and peroxisome proliferator-activated receptor pathways (Figure 7A). Analysis of the cellular origin of the regulated transcripts showed that SAA1 responses mainly stemmed from myeloid cells, while LPS primarily activated ASPCs and vascular cells, findings that were similar in the validation cohort (Figures 7C and S7A). The observation that SAA1 targets myeloid cells was further supported by the finding that Adipo^{SAA} cells marked by CES1 were positioned near macrophages in epiploic WAT and that *CES1* mRNA levels correlated with adipose macrophage abundance in an independent cohort[7] (Figures 7D, S7B, and S7C). Taken together, our results suggest that adipocyte-derived SAA1 promotes immune responses in myeloid cells within the adipose tissue microenvironment.

DISCUSSION

Most studies comparing subcutaneous and visceral fat depots have focused on omental WAT, largely because of its accessibility during intra-abdominal surgery. However, omental fat represents only a small fraction of the total visceral adipose tissue in the abdominal cavity. By systematically analyzing subcutaneous and multiple intra-abdominal fat depots, we uncover significant inter-regional differences in cellular composition and tissue architecture. For example, we identify distinct mesothelial subtypes, variations in immune and fat cell landscapes, and region-specific adipogenic niches. These findings underscore the need for caution when extrapolating ''visceral'' results from the omental depot alone.

The results presented here are based on integrative analyses of snRNA-seq and STx, requiring the development of bioinformatic approaches to extract cytoarchitectural insights from WAT—a tissue that is histologically less organized than, for example, the brain or liver. Using these scripts, we reveal a higher degree of tissue organization than previously recognized. For example, we identify region-specific enrichment of CD55^{+} mesenchymal stem cells, localized within mesothelial regions of visceral WAT or the reticular interstitium of subcutaneous WAT. The latter is consistent with findings in mice and humans.[20,22] Building on these observations, we map concentric waves of intermediate and CPAs emerging from these regions and progressing toward mature adipocytes. Additionally, we characterize immune cell-dense regions where specific leukocytes are closely positioned to one another. These findings suggest that semi-supervised clustering approaches, informed by our results, could further uncover cytoarchitectural structures in WAT, as seen in studies of the prefrontal cortex.[42]

The enrichment of Adipo^{SAA} and specific immune cells in visceral fat depots near the colon, combined with our cell-cell communication analyses predicting interactions between these cells, led us to further validate our findings. SAA1 and SAA2 are acute-phase proteins primarily produced by the liver in response to inflammation, infection, or tissue injury and are linked to obesity, atherosclerosis, inflammatory bowel disease, and cancer.[43–45] We demonstrate that recombinant SAA promotes immune responses, particularly in adipose-resident myeloid cells. Additionally, inflammatory stimuli such as LPS specifically induce *SAA1* and *SAA2* expression in fat cells, suggesting a bidirectional crosstalk in which inflammatory signals amplify immune responses through SAA1. This aligns with previous findings showing that adipocyte SAA1 and SAA2 levels correlate with macrophage infiltration[46] and that SAA1 plays a role in intestinal immunity.[26] Given that obesity is associated with increased gut permeability, allowing microbial components to enter the circulation,[31,47,48] our findings suggest that this signaling axis in WAT may serve as a response mechanism to environmental cues.

(D) Relative expression of *SAA1* (left) and *SAA2* (right) mRNA in adipocytes, ASPCs, adipose-derived endothelial cells (adECs), and THP1-derived macrophages (THP1 M0). Significant (<0.05) *p* values compared with the cell-type-specific control from one-way ANOVA are shown.
(E) Results from ELISA measurements of SAA in conditioned media from human adipocytes incubated without or with LPS for 72 h. Results are displayed as mean, error bars represent standard error of the mean, and statistical significance was calculated using Student's *t* test.
(F) Analyses of DNA methylation in the indicated cell classes for the promoter and gene body regions of *SAA1* and *SAA2*, respectively. Chromosomal localization and motifs for NFKB2/RELA/REL and STAT3 are indicated for both genes.
(G) *SAA1* and *SAA2* mRNA expression in adipocytes treated with or without LPS in the presence or absence of different inhibitors described in the main text. Data are presented as FC over vehicle. Significant (<0.05) *p* values compared with the vehicle from one-way ANOVA are shown.
For (C), (D), and (G), data are displayed as geometric mean ± 95% confidence intervals with technical replicates displayed from three independent experiments. ASPC, adipose stromal and progenitor cell.

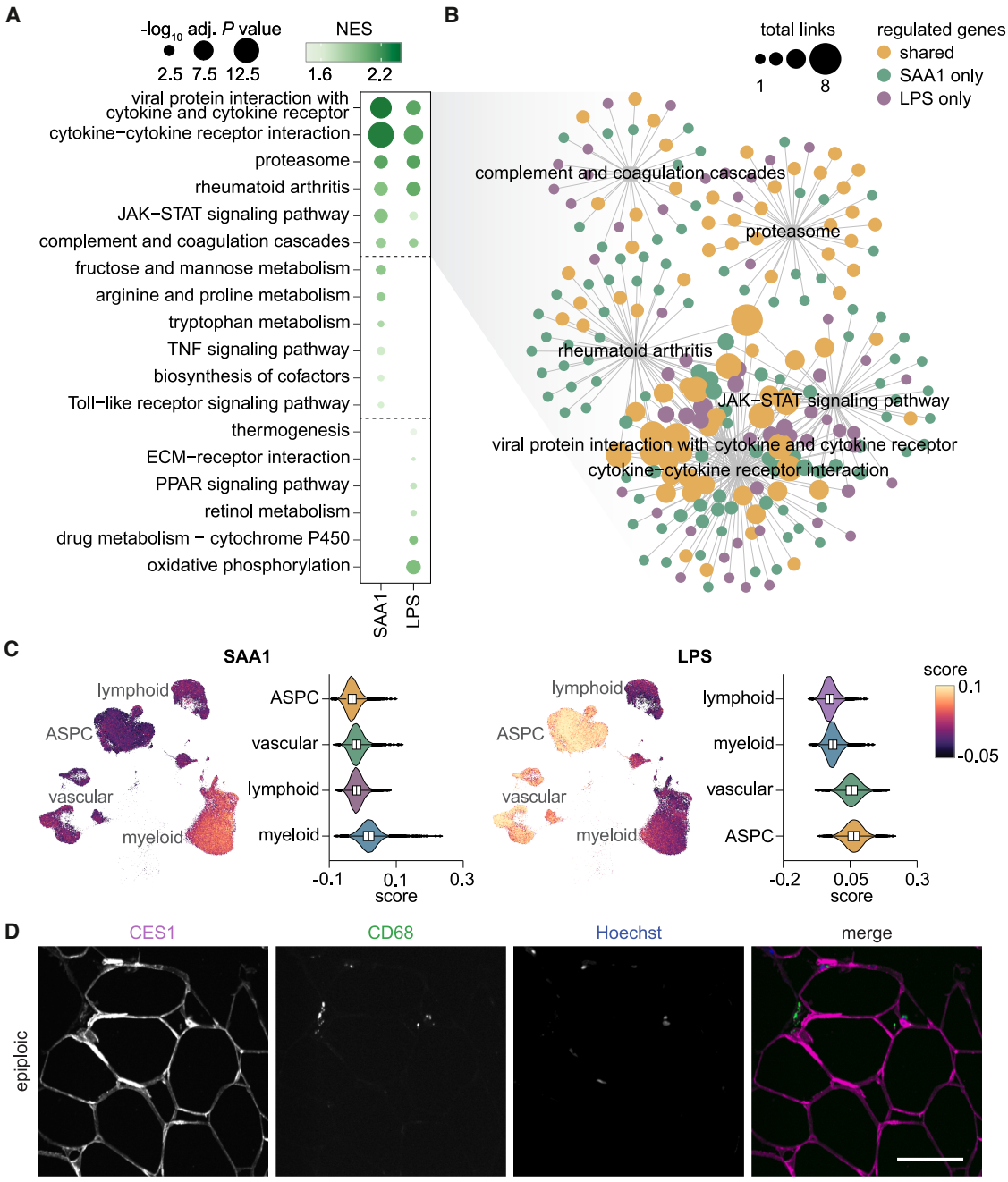

Figure 7. SAA1 activates adipose-resident myeloid cells

(A) Top Kyoto Encyclopedia of Genes and Genomes (KEGG) pathways based on differentially expressed genes from comparisons of SAA1- or LPS-treated vs. control-treated adipose-derived stromal-vascular cells.

(B) Network view of the six common SAA1- and LPS-regulated pathways showing shared and treatment-specific genes.

(C) Expression scores for SAA1- (left) and LPS-responsive (right) genes following a 6-h incubation with either ligand in stromal-vascular cells from subcutaneous human WAT. Results are displayed on the uniform manifold approximation and projection panel from Figure 1C and violin plots for each indicated cell class. Note that adipocytes and mesothelial cells were removed as these are not present in the stromal-vascular fraction from the subcutaneous depot.

(D) Representative immunostaining of epiploic adipose tissue using antibodies directed against markers for Adipo^{SAA} (CES1) and macrophages (CD68). Hoechst33342 was used as the counterstain for nuclei. Scale bar, 100 μm.

ASPC, adipose stromal and progenitor cell; NES, normalized enrichment score.

In this and our previous studies,[12,13] we use the terms Adipo^{LEP}, Adipo^{PLIN}, and Adipo^{SAA} to define adipocyte identities reproducibly observed in STx data from human WAT. However, it remains unclear whether these represent stable states or transient adaptations. As *SAA1* and *SAA2* are induced by TNF-α and LPS, our data suggest that at least Adipo^{SAA} may represent a transient, inflammation-induced state of adipocytes. Mechanistically, the LPS-mediated induction was restricted to adipocytes and required NF-κB and STAT3 signaling. In line with this, the *SAA1* and *SAA2* promoters are hypomethylated in adipocytes and harbor binding motifs for these transcription factors, providing a chromatin environment permissive for activation.

Altogether, our study provides a detailed characterization of five human WAT depots, revealing distinct regional differences in cellular composition and cytoarchitecture. We show that adipose tissue is more structured than previously thought and identify an adipocyte-immune signaling axis active in colon-associated fat depots. As all our data will be made available through public repositories, including the adipose tissue knowledge portal (http://www.adiposetissue.org/),[18] they allow for additional in-depth analyses of single-cell and spatial aspects of WAT biology.

Limitations of the study

Testing the mechanistic basis of adipocyte *SAA* induction in humans would ideally require repeated visceral fat biopsies before and after specific interventions, which are not practically or ethically feasible. Moreover, such experiments cannot be replicated in mice because of fundamental interspecies differences in fat distribution and anatomy, including the absence of epiploic WAT.[49] Another limitation is that all tissue samples in this study were derived from individuals with obesity. While this provided access to otherwise inaccessible adipose depots and enabled analyses in two independent cohorts, it constrains direct comparisons with normal-weight individuals and may limit the generalizability of our findings to the broader population.

RESOURCE AVAILABILITY

Lead contact

Further information and requests for resources and reagents should be directed to and will be fulfilled by the lead contact, Niklas Mejhert (niklas.mejhert@ki.se).

Materials availability

All unique reagents generated in this study are available from the lead contact upon request.

Data and code availability

Raw data are provided in Data S1. Spatial and single-nuclei RNA sequencing data are deposited at Mendeley Data (https://doi.org/10.17632/8p7k6htgfm.1). All R scripts are deposited at GitHub (https://github.com/jiawei-zhong/WAT_depots). Any additional information required to reanalyze the data reported in this paper is available from the lead contact upon request. However, full individual clinical data are not publicly available because these data contain information that could compromise research participant privacy or consent.

ACKNOWLEDGMENTS

We thank Dr. David Rojas Márquez (http://darwidillustration.com/en/) for the scientific illustration in Figure 1A and the following infrastructures at Karolinska Institutet for support: the Centre for Bioinformatics and Biostatistics (computational) and the Live Cell Imaging Core facility/Nikon Center of Excellence (imaging). We also thank Ms. Beate Gutsmann for her valuable technical help processing the clinical samples and Dr. Martin Gericke for his feedback on anatomical descriptions of the depots. We thank Anton Gulko for help with processing the US cohort samples and the staff at Ersta Hospital (CRC) for providing adipose tissue biopsies. This work was supported by grants from the Swedish Research Council (L.M., M.R., N.M., and P.L.S.), the Novo Nordisk Foundation (M.R. and N.M.), Knut and Alice Wallenberg Foundation (Clinical Scholar to M.R. and Academy Fellow to N.M.), CIMED (M.R. and N.M.), the Strategic Research Program in Diabetes at Karolinska Institutet (M.R. and N.M.), the European Foundation for the Study of Diabetes (L.M. and N.M.), ERC-SyG SPHERES (M.R.), the German Diabetes Association (L.M.), the Swedish Diabetes Foundation (M.R.), the Stockholm County Council (M.R.), Konung Gustaf V:s och Drottning Victorias Stiftelse (M.R.), The Erling-Persson Foundation (A.T.), and a Consolidator grant from Karolinska Institutet (N.M.). M.P.E. was supported by NIH grant K01DK134806. E.D.R. was supported by NIH grant RC2 DK116691, and US sequencing was performed by the BIDMC Functional Genomics and Bioinformatics core, which is funded by NIH grant P30DK135043.

AUTHOR CONTRIBUTIONS

J.J., L.M., M.R., and N.M. conceived the study. J.J., M.R., and N.M. wrote the first draft of the manuscript. A.D., A.T., J.B., L.M., M. Blüher, and P.K. organized sample collection and provided intellectual input to shape the study design. J.J., J.Z., L.M., and P.A.N.N. generated and/or analyzed the snRNA-seq data. B.P., J.J., J.L., J.Z., L.M., N.B., and P.L.S. generated and/or analyzed the STx data. W.G. and A.C. collected surgical samples for the validation cohort. E.D.R., M.P.E., and Z.Y.L. conceived, performed, and analyzed data from the validation cohort. J.J. and S.W. performed and analyzed the *in vitro* experiments, and J.J., M.E., and S.F.-C. performed the immunostaining experiments. J.K. and M. Buggert provided key input for the cell annotations and design of the cell experiments. All authors read and approved the final version of the manuscript.

DECLARATION OF INTERESTS

M. Blüher and M.R. received honoraria as consultants and/or speakers from Amgen, AstraZeneca, Bayer, Boehringer Ingelheim, Daiichi-Sankyo (only M. Blüher), Eli Lilly, Novo Nordisk, Novartis, and Sanofi. E.D.R. is on the Scientific Advisory Board of Source Bio, Inc. and received honoraria from Gensaic and Foghorn Therapeutics.

STAR★METHODS

Detailed methods are provided in the online version of this paper and include the following:

- KEY RESOURCES TABLE
- EXPERIMENTAL MODEL AND STUDY PARTICIPANT DETAILS
- METHOD DETAILS
  - Spatial transcriptomics using Visium spatial gene expression
  - Preprocessing of spatial transcriptomic data
  - Spatial data integration and cell type identification
  - Generation of single-nucleus RNA sequencing data
  - Preprocessing of snRNA-seq data
  - snRNA-seq data integration and cell type identification
  - Data generation and processing of the validation cohort
  - Spatial deconvolution
  - Quantifying spatial neighborhood enrichment with *SENSE*
  - Pseudo-time analysis
  - Cell-cell communication analysis
  - Bulk deconvolution
  - IHC staining and imaging
  - Quantification of CES1 signal
  - Human adipose tissue-derived stromal cell differentiation and stimulation

- Adipose tissue-derived endothelial cell isolation and culture
- THP1 cell culture
- Magnetic bead separation and LPS stimulation of $CD45^+$ cells
- Gene expression analysis by quantitative reverse transcription PCR
- Western blot
- SAA quantification in conditioned media
- Stromal-vascular fraction isolation for LPS and recombinant SAA treatment
- Bulk RNA-seq data analysis of LPS and recombinant SAA treated samples
- Gene set enrichment analysis

- QUANTIFICATION AND STATISTICAL ANALYSIS

SUPPLEMENTAL INFORMATION

Supplemental information can be found online at https://doi.org/10.1016/j.cmet.2025.12.008.

Received: April 1, 2025
Revised: October 3, 2025
Accepted: December 10, 2025
Published: January 13, 2026

REFERENCES

1. Sakers, A., De Siqueira, M.K., Seale, P., and Villanueva, C.J. (2022). Adipose-tissue plasticity in health and disease. Cell *185*, 419–446. https://doi.org/10.1016/J.CELL.2021.12.016.
2. Emont, M.P., Jacobs, C., Essene, A.L., Pant, D., Tenen, D., Colleluori, G., Di Vincenzo, A., Jørgensen, A.M., Dashti, H., Stefek, A., et al. (2022). A single-cell atlas of human and mouse white adipose tissue. Nature *7903*, 926–933. https://doi.org/10.1038/s41586-022-04518-2.
3. Belligoli, A., Compagnin, C., Sanna, M., Favaretto, F., Fabris, R., Busetto, L., Foletto, M., Dal Prà, C., Serra, R., Prevedello, L., et al. (2019). Characterization of subcutaneous and omental adipose tissue in patients with obesity and with different degrees of glucose impairment. Sci. Rep. *9*, 11333. https://doi.org/10.1038/s41598-019-47719-y.
4. Vijay, J., Gauthier, M.F., Biswell, R.L., Louiselle, D.A., Johnston, J.J., Cheung, W.A., Belden, B., Pramatarova, A., Biertho, L., Gibson, M., et al. (2019). Single-cell analysis of human adipose tissue identifies depot- and disease-specific cell types. Nat. Metab. *2*, 97–109. https://doi.org/10.1038/s42255-019-0152-6.
5. Zhang, H., Ding, Y., Zeng, Q., Wang, D., Liu, G., Hussain, Z., Xiao, B., Liu, W., and Deng, T. (2022). Characteristics of mesenteric adipose tissue attached to different intestinal segments and their roles in immune regulation. Am. J. Physiol., Gastrointest. Liver Physiol. *322*, G310–G326. https://doi.org/10.1152/ajpgi.00256.2021.
6. Wu, Z., Tan, J., Chi, Y., Zhang, F., U., J., Song, Y., Cong, U., Wu, N., and Liu, Y. (2018). Mesenteric adipose tissue contributes to intestinal barrier integrity and protects against nonalcoholic fatty liver disease in mice. Am. J. Physiol., Gastrointest. Liver Physiol. *315*, G659–G670. https://doi.org/10.1152/AJPGI.00079.2018/ASSET/IMAGES/LARGE/ZH30081874800007.JPEG.
7. Krieg, L., Didt, K., Karkossa, I., Bernhart, S.H., Kehr, S., Subramanian, N., Lindhorst, A., Schaudinn, A., Tabei, S., Keller, M., et al. (2022). Multiomics reveal unique signatures of human epiploic adipose tissue related to systemic insulin resistance. Gut *71*, 2179–2193. https://doi.org/10.1136/GUTJNL-2021-324603.
8. Ni, Z., Prasad, A., Chen, S., Halberg, R.B., Arkin, L.M., Drolet, B.A., Newton, M.A., and Kendziorski, C. (2022). SpotClean adjusts for spot swapping in spatial transcriptomics data. Nat. Commun. *13*, 2971. https://doi.org/10.1038/s41467-022-30587-y.
9. Korsunsky, I., Millard, N., Fan, J., Slowikowski, K., Zhang, F., Wei, K., Baglaenko, Y., Brenner, M., Loh, P.R., and Raychaudhuri, S. (2019). Fast, sensitive and accurate integration of single-cell data with Harmony. Nat. Methods *16*, 1289–1296. https://doi.org/10.1038/s41592-019-0619-0.
10. Lopez, R., Regier, J., Cole, M.B., Jordan, M.I., and Yosef, N. (2018). Deep generative modeling for single-cell transcriptomics. Nat. Methods *15*, 1053–1058. https://doi.org/10.1038/s41592-018-0229-2.
11. Luecken, M.D., Büttner, M., Chaichoompu, K., Danese, A., Interlandi, M., Mueller, M.F., Strobl, D.C., Zappia, L., Dugas, M., Colomé-Tatché, M., et al. (2021). Benchmarking atlas-level data integration in single-cell genomics. Nat. Methods *19*, 41–50. https://doi.org/10.1038/s41592-021-01336-8.
12. Bäckdahl, J., Franzén, L., Massier, L., Li, Q., Jalkanen, J., Gao, H., Andersson, A., Bhalla, N., Thorell, A., Rydén, M., et al. (2021). Spatial mapping reveals human adipocyte subpopulations with distinct sensitivities to insulin. Cell Metab. *33*, 1869–1882.e6. https://doi.org/10.1016/J.CMET.2021.07.018.
13. Massier, L., Jalkanen, J., Elmastas, M., Zhong, J., Wang, T., Nono Nankam, P.A., Frendo-Cumbo, S., Bäckdahl, J., Subramanian, N., Sekine, T., et al. (2023). An integrated single cell and spatial transcriptomic map of human white adipose tissue. Nat. Commun. *14*, 1438. https://doi.org/10.1038/S41467-023-36983-2.
14. Ferrero, R., Rainer, P.Y., Rumpler, M., Russeil, J., Zachara, M., Pezoldt, J., van Mierlo, G., Gardeux, V., Saelens, W., Alpern, D., et al. (2024). A human omentum-specific mesothelial-like stromal population inhibits adipogenesis through IGFBP2 secretion. Cell Metab. *36*, 1566–1585.e9. https://doi.org/10.1016/j.cmet.2024.04.017.
15. Acosta, J.R., Joost, S., Karlsson, K., Ehrlund, A., Li, X., Aouadi, M., Kasper, M., Arner, P., Rydén, M., and Laurencikiene, J. (2017). Single cell transcriptomics suggest that human adipocyte progenitor cells constitute a homogeneous cell population. Stem Cell Res. Ther. *8*, 1–6. https://doi.org/10.1186/S13287-017-0701-4/FIGURES/2.
16. Ehrlund, A., Mejhert, N., Björk, C., Andersson, R., Kulyté, A., Åström, G., Itoh, M., Kawaji, H., Lassmann, T., Daub, C.O., et al. (2017). Transcriptional dynamics during human adipogenesis and its link to adipose morphology and distribution. Diabetes *66*, 218–230. https://doi.org/10.2337/DB16-0631.
17. Noguchi, S., Arakawa, T., Fukuda, S., Furuno, M., Hasegawa, A., Hori, F., Ishikawa-Kato, S., Kaida, K., Kaiho, A., Kanamori-Katayama, M., et al. (2017). FANTOM5 CAGE profiles of human and mouse samples. Sci. Data *4*, 170112. https://doi.org/10.1038/sdata.2017.112.
18. Zhong, J., Zareifi, D., Weinbrenner, S., Hansen, M., Klingelhuber, F., Nono Nankam, P.A., Frendo-Cumbo, S., Bhalla, N., Cordeddu, L., de Castro Barbosa, T., et al. (2025). adiposetissue.org: A knowledge portal integrating clinical and experimental data from human adipose tissue. Cell Metab. *37*, 566–569. https://doi.org/10.1016/J.CMET.2025.01.012.
19. Kleshchevnikov, V., Shmatko, A., Dann, E., Aivazidis, A., King, H.W., Li, T., Elmentaite, R., Lomakin, A., Kedlian, V., Gayoso, A., et al. (2022). Cell2location maps fine-grained cell types in spatial transcriptomics. Nat. Biotechnol. *40*, 661–671. https://doi.org/10.1038/s41587-021-01139-4.
20. Merrick, D., Sakers, A., Irgebay, Z., Okada, C., Calvert, C., Morley, M.P., Percec, I., and Seale, P. (2019). Identification of a mesenchymal progenitor cell hierarchy in adipose tissue. Science *364*, eaav2501. https://doi.org/10.1126/science.aav2501.
21. Benias, P.C., Wells, R.G., Sackey-Aboagye, B., Klavan, H., Reidy, J., Buonocore, D., Miranda, M., Kornacki, S., Wayne, M., Carr-Locke, D.L., et al. (2018). Structure and distribution of an unrecognized interstitium in human tissues. Sci. Rep. *8*, 4947. https://doi.org/10.1038/s41598-018-23062-6.
22. Uhrbom, M., Muhl, L., Genové, G., Liu, J., Palmgren, H., Alexandersson, I., Karlsson, F., Zhou, A.X., Lunnerdal, S., Gustafsson, S., et al. (2024). Adipose stem cells are sexually dimorphic cells with dual roles as preadipocytes and resident fibroblasts. Nat. Commun. *15*, 7643. https://doi.org/10.1038/s41467-024-51867-9.
23. Klingelhuber, F., Frendo-Cumbo, S., Omar-Hmeadi, M., Massier, L., Kakimoto, P., Taylor, A.J., Couchet, M., Ribicic, S., Wabitsch, M.,

Messias, A.C., et al. (2024). A spatiotemporal proteomic map of human adipogenesis. Nat. Metab. *6*, 861–879. https://doi.org/10.1038/S42255-024-01025-8.

24. Weiler, P., Lange, M., Klein, M., Pe'er, D., and Theis, F. (2024). CellRank 2: unified fate mapping in multiview single-cell data. Nat. Methods *21*, 1196–1205. https://doi.org/10.1038/s41592-024-02303-9.
25. Jin, S., Plikus, M.V., and Nie, Q. (2024). CellChat for systematic analysis of cell–cell communication from single-cell transcriptomics. Nat. Protoc. *20*, 180–219. https://doi.org/10.1038/s41596-024-01045-4.
26. Bang, Y.J., Hu, Z., Li, Y., Gattu, S., Ruhn, K.A., Raj, P., Herz, J., and Hooper, L.V. (2021). Serum amyloid a delivers retinol to intestinal myeloid cells to promote adaptive immunity. Science *373*, eabf9232. https://doi.org/10.1126/science.abf9232.
27. Cheng, N., He, R., Tian, J., Ye, P.P., and Ye, R.D. (2008). Cutting Edge: TLR2 is a functional receptor for acute-phase serum amyloid A. J. Immunol. *181*, 22–26. https://doi.org/10.4049/JIMMUNOL.181.1.22.
28. Su, S.B., Gong, W., Gao, J.L., Shen, W., Murphy, P.M., Oppenheim, J.J., and Wang, J.M. (1999). A seven-transmembrane, G protein–coupled receptor, FPRL1, mediates the chemotactic activity of serum amyloid A for human phagocytic cells. J. Exp. Med. *189*, 395–402. https://doi.org/10.1084/JEM.189.2.395.
29. Abouelasrar Salama, S., Gouwy, M., Van Damme, J., and Struyf, S. (2021). The turning away of serum amyloid A biological activities and receptor usage. Immunology *163*, 115–127. https://doi.org/10.1111/IMM.13295.
30. Massier, L., Chakaroun, R., Tabei, S., Crane, A., Didt, K.D., Fallmann, J., Von Bergen, M., Haange, S.B., Heyne, H., Stumvoll, M., et al. (2020). Adipose tissue derived bacteria are associated with inflammation in obesity and type 2 diabetes. Gut *69*, 1796–1806. https://doi.org/10.1136/GUTJNL-2019-320118.
31. Cani, P.D., Amar, J., Iglesias, M.A., Poggi, M., Knauf, C., Bastelica, D., Neyrinck, A.M., Fava, F., Tuohy, K.M., Chabo, C., et al. (2007). Metabolic endotoxemia initiates obesity and insulin resistance. Diabetes *56*, 1761–1772. https://doi.org/10.2337/DB06-1491.
32. Schnedl, W.J., Krause, R., Tafeit, E., Tillich, M., Lipp, R.W., and Wallner-Liebmann, S.J. (2010). Insights into epiploic appendagitis. Nat. Rev. Gastroenterol. Hepatol. *1*, 45–49. https://doi.org/10.1038/nrgastro.2010.189.
33. Batra, A., Heimesaat, M.M., Bereswill, S., Fischer, A., Glauben, R., Kunkel, D., Scheffold, A., Erben, U., Kühl, A., Loddenkemper, C., et al. (2012). Mesenteric fat—control site for bacterial translocation in colitis? Mucosal Immunol. *5*, 580–591. https://doi.org/10.1038/mi.2012.33.
34. Nakarai, H., Yamashita, A., Nagayasu, S., Iwashita, M., Kumamoto, S., Ohyama, H., Hata, M., Soga, Y., Kushiyama, A., Asano, T., et al. (2012). Adipocyte-macrophage interaction may mediate LPS-induced low-grade inflammation: Potential link with metabolic complications. Innate Immun. *18*, 164–170. https://doi.org/10.1177/1753425910393370.
35. Chen, Z.J., Das, S.S., Kar, A., Lee, S.H.T., Abuhanna, K.D., Alvarez, M., Sukhatme, M.G., Wang, Z., Gelev, K.Z., Heffel, M.G., et al. (2025). Single-cell DNA methylome and 3D genome atlas of human subcutaneous adipose tissue. Nat. Genet. *57*, 2238–2249. https://doi.org/10.1038/s41588-025-02300-4.
36. Zhang, S.C., Wang, M.Y., Feng, J.R., Chang, Y., Ji, S.R., and Wu, Y. (2020). Reversible promoter methylation determines fluctuating expression of acute phase proteins. eLife *9*, e51317. https://doi.org/10.7554/ELIFE.51317.
37. Han, S.J., Ko, H.M., Choi, J.H., Seo, K.H., Lee, H.S., Choi, E.K., Choi, I.W., Lee, H.K., and Im, S.Y. (2002). Molecular mechanisms for lipopolysaccharide-induced biphasic activation of nuclear factor-κB (NF-κB). J. Biol. Chem. *277*, 44715–44721. https://doi.org/10.1074/jbc.M202524200.
38. Meng, A., Zhang, X., and Shi, Y. (2014). Role of p38 MAPK and STAT3 in lipopolysaccharide-stimulated mouse alveolar macrophages. Exp. Ther. Med. *8*, 1772–1776. https://doi.org/10.3892/ETM.2014.2023.
39. Bollrath, J., and Greten, F.R. (2009). IKK/NF-B and STAT3 pathways: Central signalling hubs in inflammation-mediated tumour promotion and metastasis. EMBO Rep. *10*, 1314–1319. https://doi.org/10.1038/EMBOR.2009.243/ASSET/DB326E80-D2B8-4E17-868A-F53E27CF4BBC/ASSETS/GRAPHIC/EMBR2009243-FIG-0003-M.JPG.
40. Lee, H., Herrmann, A., Deng, J.H., Kujawski, M., Niu, G., Li, Z., Forman, S., Jove, R., Pardoll, D.M., and Yu, H. (2009). Persistently activated Stat3 maintains constitutive NF-κB activity in tumors. Cancer Cell *15*, 283–293. https://doi.org/10.1016/j.ccr.2009.02.015.
41. Ahuja, A., Kim, E., Sung, G.H., and Cho, J.Y. (2020). STAT3 differentially regulates TLR4-mediated inflammatory responses in early or late phases. Int. J. Mol. Sci. *21*, 7675. https://doi.org/10.3390/IJMS21207675.
42. Maynard, K.R., Collado-Torres, L., Weber, L.M., Uytingco, C., Barry, B.K., Williams, S.R., Catallini, J.L., Tran, M.N., Besich, Z., Tippani, M., et al. (2021). Transcriptome-scale spatial gene expression in the human dorsolateral prefrontal cortex. Nat. Neurosci. *24*, 425–436. https://doi.org/10.1038/s41593-020-00787-0.
43. Chang, Y., Liu, Y., Zou, Y., and Ye, R.D. (2025). Recent advances in studies of serum amyloid A: implications in inflammation, immunity and tumor metastasis. Int. J. Mol. Sci. *26*, 987. https://doi.org/10.3390/IJMS26030987.
44. Chen, R., Chen, Q., Zheng, J., Zeng, Z., Chen, M., Li, L., and Zhang, S. (2023). Serum amyloid protein A in inflammatory bowel disease: from bench to bedside. Cell Death Discov. *9*, 154. https://doi.org/10.1038/s41420-023-01455-5.
45. Sack, G.H. (2018). Serum amyloid A – a review. Mol. Med. *24*, 46. https://doi.org/10.1186/S10020-018-0047-0.
46. Poitou, C., Divoux, A., Faty, A., Tordjman, J., Hugol, D., Aissat, A., Keophiphath, M., Henegar, C., Commans, S., and Clément, K. (2009). Role of serum amyloid A in adipocyte-macrophage cross talk and adipocyte cholesterol efflux. J. Clin. Endocrinol. Metab. *94*, 1810–1817. https://doi.org/10.1210/JC.2008-2040.
47. Damms-Machado, A., Louis, S., Schnitzer, A., Volynets, V., Rings, A., Basrai, M., and Bischoff, S.C. (2017). Gut permeability is related to body weight, fatty liver disease, and insulin resistance in obese individuals undergoing weight reduction. Am. J. Clin. Nutr. *105*, 127–135. https://doi.org/10.3945/AJCN.116.131110.
48. Frazier, T.H., DiBaise, J.K., and McClain, C.J. (2011). Gut microbiota, intestinal permeability, obesity-induced inflammation, and liver injury. JPEN J. Parenter. Enteral Nutr. *35*, 14S–20S. https://doi.org/10.1177/0148607111413772.
49. Börgeson, E., Boucher, J., and Hagberg, C.E. (2022). Of mice and men: Pinpointing species differences in adipose tissue biology. Front. Cell Dev. Biol. *10*, 1003118. https://doi.org/10.3389/fcell.2022.1003118.
50. Young, M.D., and Behjati, S. (2020). SoupX removes ambient RNA contamination from droplet-based single-cell RNA sequencing data. GigaScience *9*, giaa151. https://doi.org/10.1093/GIGASCIENCE/GIAA151.
51. McGinnis, C.S., Murrow, L.M., and Gartner, Z.J. (2019). DoubletFinder: doublet detection in single-cell RNA sequencing data using artificial nearest neighbors. Cell Syst. *8*, 329–337.e4. https://doi.org/10.1016/J.CELS.2019.03.003.
52. Martin, M. (2011). Cutadapt removes adapter sequences from high-throughput sequencing reads. EMBnet J. *17*, 10–12. https://doi.org/10.14806/EJ.17.1.200.
53. Hao, Y., Hao, S., Andersen-Nissen, E., Mauck, W.M., Zheng, S., Butler, A., Lee, M.J., Wilk, A.J., Darby, C., Zager, M., et al. (2021). Integrated analysis of multimodal single-cell data. Cell *184*, 3573–3587.e29. https://doi.org/10.1016/J.CELL.2021.04.048.
54. Gaublomme, J.T., Li, B., McCabe, C., Knecht, A., Yang, Y., Drokhlyansky, E., Van Wittenberghe, N., Waldman, J., Dionne, D., Nguyen, L., et al. (2019). Nuclei multiplexing with barcoded antibodies for single-nucleus genomics. Nat. Commun. *10*, 2907. https://doi.org/10.1038/s41467-019-10756-2.
55. Fleming, S.J., Chaffin, M.D., Arduini, A., Akkad, A.D., Banks, E., Marioni, J.C., Philippakis, A.A., Ellinor, P.T., and Babadi, M. (2023). Unsupervised removal of systematic background noise from droplet-based single-cell

experiments using CellBender. Nat. Methods *20*, 1323–1335. https://doi.org/10.1038/s41592-023-01943-7.

56. Bais, A.S., and Kostka, D. (2020). scds: computational annotation of doublets in single-cell RNA sequencing data. Bioinformatics *36*, 1150–1158. https://doi.org/10.1093/BIOINFORMATICS/BTZ698.
57. Germain, P.L., Robinson, M.D., Lun, A., Garcia Meixide, C., and Macnair, W. (2022). Doublet identification in single-cell sequencing data using *scDblFinder*. F1000Research *10*, 979. https://doi.org/10.12688/f1000research.73600.2.
58. Jew, B., Alvarez, M., Rahmani, E., Miao, Z., Ko, A., Garske, K.M., Sul, J.H., Pietiläinen, K.H., Pajukanta, P., and Halperin, E. (2020). Accurate estimation of cell composition in bulk expression through robust integration of single-cell information. Nat. Commun. *11*, 1971. https://doi.org/10.1038/s41467-020-15816-6.
59. Dobin, A., Davis, C.A., Schlesinger, F., Drenkow, J., Zaleski, C., Jha, S., Batut, P., Chaisson, M., and Gingeras, T.R. (2013). STAR: ultrafast universal RNA-seq aligner. Bioinformatics *29*, 15–21. https://doi.org/10.1093/BIOINFORMATICS/BTS635.
60. Anders, S., Pyl, P.T., and Huber, W. (2015). HTSeq—a Python framework to work with high-throughput sequencing data. Bioinformatics *31*, 166–169. https://doi.org/10.1093/BIOINFORMATICS/BTU638.
61. Mudge, J.M., Carbonell-Sala, S., Diekhans, M., Martinez, J.G., Hunt, T., Jungreis, I., Loveland, J.E., Arnan, C., Barnes, I., Bennett, R., et al. (2025). GENCODE 2025: reference gene annotation for human and mouse. Nucleic Acids Res. *53*, D966–D975. https://doi.org/10.1093/NAR/GKAE1078.
62. Yu, G., Wang, L.G., Han, Y., and He, Q.Y. (2012). ClusterProfiler: An R package for comparing biological themes among gene clusters. Omics *16*, 284–287. https://doi.org/10.1089/omi.2011.0118.
63. Love, M.I., Huber, W., and Anders, S. (2014). Moderated estimation of fold change and dispersion for RNA-seq data with DESeq2. Genome Biol. *15*, 1–21. https://doi.org/10.1186/S13059-014-0550-8/FIGURES/9.
64. Gulko, A., Essene, A., Belmont-Rausch, D.M., Veregge, M., Pant, D., Tenen, D., Kapel, B.S., Emont, M.P., Pers, T.H., Rosen, E.D., et al. (2024). Protocol for flow cytometry-assisted single-nucleus RNA sequencing of human and mouse adipose tissue with sample multiplexing. Star Protoc. *5*, 102893. https://doi.org/10.1016/J.XPRO.2024.102893.
65. Couchet, M., Gao, H., Klingelhuber, F., Jalkanen, J., De Castro Barbosa, T.D.C., Omar-Hmeadi, M., Massier, L., Krahmer, N., Mejhert, N., and Rydén, M. (2025). Adipogenic characterization of immortalized CD55+ progenitor cells from human white adipose tissue. Adipocyte *14*, 2283213. https://doi.org/10.1080/21623945.2023.2283213.
66. Herold, J., and Kalucka, J. (2022). A rapid adaptable method for isolation of endothelial cells from human adipose tissue. Methods Mol. Biol. *2441*, 235–250. https://doi.org/10.1007/978-1-0716-2059-5_18.
67. Livak, K.J., and Schmittgen, T.D. (2001). Analysis of relative gene expression data using real-time quantitative PCR and the 2-ΔΔCT method. Methods *25*, 402–408. https://doi.org/10.1006/METH.2001.1262.
68. van Harmelen, V., Skurk, T., and Hauner, H. (2005). Primary culture and differentiation of human adipocyte precursor cells. Methods Mol. Med. *107*, 125–135. https://doi.org/10.1385/1-59259-861-7:125.

STAR★METHODS

KEY RESOURCES TABLE

REAGENT or RESOURCE	SOURCE	IDENTIFIER
Antibodies		
CES1 polyclonal antibody	Proteintech	Cat#16912-1-AP; RRID:AB_2077500
KRT19 monoclonal antibody (EP1580Y)	Abcam	Cat#ab52625; RRID:AB_2281020
CD68 multiclonal antibody	Abcam	Cat#ab199000; RRID: AB_3720205
Donkey anti-rabbit secondary antibody conjugated with Alexa Fluor 647	Thermo Fisher Scientific	Cat#A-31573; RRID:AB_2536183
Donkey anti-rabbit secondary antibody conjugated with Alexa Fluor 555	Thermo Fisher Scientific	Cat#A-31572; RRID:AB_162543
Donkey anti-mouse secondary antibody conjugated with Alexa Fluor 488	Thermo Fisher Scientific	Cat#A-21202; RRID:AB_141607
CD284 (TLR4) monoclonal antibody (HTA125)	eBioscience	Cat#14-9917-82; RRID:AB_468607
CD14 monoclonal antibody (61D3)	eBioscience	Cat#14-0149-82; RRID:AB_467129
NFκB p65 monoclonal antibody (D14E12)	Cell Signaling	Cat#8242; RRID:AB_10859369
Phospho-NFκB p65 [Ser536] monoclonal antibody (93H1)	Cell Signaling	Cat#3033; RRID:AB_331284
STAT3 monoclonal antibody (124H6)	Cell Signaling	Cat#9139; RRID:AB_331757
Phospho-STAT3 [Tyr705] monoclonal antibody (D3A7)	Cell Signaling	Cat#9145; RRID:AB_2491009
α-tubulin monoclonal antibody (11H10)	Cell Signaling	Cat#2125; RRID:AB_2619646
Anti-rabbit IgG, HRP-linked antibody	Cell Signaling	Cat#7074; RRID:AB_2099233
Anti-Mouse IgG, HRP-linked antibody	Promega	Cat#W4021; RRID:AB_430834
Biological samples		
Human subcutaneous and visceral adipose tissue samples, main cohort	Leipzig Obesity Biobank	https://www.helmholtz-munich.de/en/hi-mag/cohort/leipzig-obesity-bio-bank-lobb
Human subcutaneous and visceral adipose tissue samples, validation cohort	This paper	N/A
Human subcutaneous adipose tissue samples	This paper	N/A
Chemicals, peptides, and recombinant proteins		
Serum-free protein block	Agilent Technologies	Cat#X090930-2
TrueView autofluorescence quenching kit	Vector labs	Cat#VEC-SP-8400-15
Fluorescein-labeled lectin	Vector labs	Cat#FL-1041
Dylight649-labeled lectin	Vector labs	Cat#DL-1048-1
Hoechst33342	Abcam	Cat#ab228551
VectaMount AQ Mounting Medium	Vector labs	Cat#H-5501
LPS derived from E. coli (O55:B5)	Sigma-Aldrich	Cat#L4524
Fetal bovine serum	Hyclone	Cat#SV30160
Human recombinant TNF-α protein	Sigma-Aldrich	Cat#H8916
Human recombinant IL-6 protein	Thermo Fisher Scientific	Cat#200-06
Human recombinant IL-1β protein	Sigma-Aldrich	Cat#H6291
Z-VAD-FMK	Bio-Techne	Cat#FMK001
BAY-11-7082	Sigma-Aldrich	Cat#196870
STAT3i VII	Sigma-Aldrich	Cat#573103
Phorbol-12-myristat-13-acetat (PMA)	Sigma-Aldrich	Cat#P8139
cOmplete Mini, EDTA-free Protease Inhibitor Cocktail	Sigma-Aldrich	Cat#11836170001
PhosSTOP Phosphatase Inhibitor	Sigma-Aldrich	Cat#4906837001
ECL Select reagent	Cytiva	Cat#RPN2235

(*Continued on next page*)

Continued

REAGENT or RESOURCE	SOURCE	IDENTIFIER
Human recombinant SAA1 protein	OriGene	Cat#TP310664
CD45 MicroBeads, human	Miltenyi	Cat#130-045-801
Critical commercial assays		
Human Serum Amyloid A Human ELISA Kit	Abcam	Cat#ab100635
Chromium Single Cell v3.1	10X Genomics	Cat#PN-1000691, PN-1000690, PN-1000215
Visium Spatial Gene Expression	10X Genomics	Cat#PN-1000186, PN-1000190, PN-1000185
Deposited data		
Source data	This paper	Data S1
Raw and analyzed adipose depots single nuclei and spatial gene expression data	This paper	Mendeley Data: https://doi.org/10.17632/8p7k6htgfm.1
RNA-seq matrices of adipose stromal vascular cells under SAA1 or LPS treatment	This paper	Mendeley Data: https://doi.org/10.17632/8p7k6htgfm.1
Human reference genome NCBI build 38, GRCh38	Genome Reference Consortium	https://www.ncbi.nlm.nih.gov/datasets/genome/GCF_000001405.40/
Adipose snRNA-seq data, previously published	Emont et al.[2]	GEO: GSE176067 and GSE176171
Published spatial transcriptomics of human adipose tissue	Bäckdahl et al.[12]	Mendeley Data: https://doi.org/10.17632/3bs5f8mvbs.1
Integrated sc/snRNA-seq map of human adipose	Massier et al.[13]	Mendeley Data: https://doi.org/10.17632/y3pxvr4xbf.2
FANTOM5 CAGE-seq data	Noguchi et al.[17]	https://fantom.gsc.riken.jp/5/data/
Microarray of cell type fractions of human WAT	Acosta et al.[15]	GEO: GSE100795
Proteomics data of human preadipocyte adipogenesis	Klingelhuber et al.[23]	PRIDE: PXD047412
Adipose depots validation data, transcriptomics	Krieg et al.[7]	https://doi.org/10.1136/gutjnl-2021-324603
Adipose depots validation data, proteomics	Krieg et al.[7]	PRIDE: PXD022465
Adipose snm3C-seq3 and snRNA-seq data	Chen et al.[35]	GEO: GSE297267
Experimental models: Cell lines		
THP1 cells	This paper	N/A
Adipose tissue derived endothelial cells	This paper	N/A
Adipose tissue derived stem cells	This paper	N/A
Oligonucleotides		
Primers for *SAA1;* fw: AACTATGATGCTGCCAAAAGG, rev: TGGATATTCTCTCTGGCATCG	This paper	N/A
Primers for *SAA2;* fw: CTGCAGAAGTGATCAGCA, rev: ATTATATGCCATATCTCAGC	This paper	N/A
Primers for *IL6*; fw: CCTGAACCTTCCAAAGATGGC, rev: TTCACCAGGCAAGTGTCCTCA	This paper	N/A
Primers for *CCL2*; fw: AGAATCACCAGCAGCAAGTGTCC, rev: TCCTGAACCCACTTCTGCTTGG	This paper	N/A
Primers for *CXCL8*; fw: CACTGCGCCAACACAGAAAT, rev: TTCTCAGCCCTCTTCAAAAACTTC	This paper	N/A
Primers for *PLIN1*; fw: TGGAGACTGAGGAGAACAAG, rev: ATGTCACAGCCGAGATGG	This paper	N/A
Primers for *LEP*; fw: CTGTGCGGATTCTTGTGGCT, rev: GAGGAGACTGACTGCGTGTGT	This paper	N/A
Primers for *18S*; fw: TGACTCAACACGGGAAACC, rev: TCGCTCCACCAACTAAGAAC	This paper	N/A

(*Continued on next page*)

Continued

REAGENT or RESOURCE	SOURCE	IDENTIFIER
Primers for *B2M*; fw: AAGGACTGGTCTTTCTATCTC, rev: GATCCCACTTAACTATCTTGG	This paper	N/A
Primers for *RPLP0*; fw: AACTCTGCATTCTCGCTTCC, rev: GGACTCGTTTGTACCCGTTG	This paper	N/A
Software and algorithms		
Code for data analysis	This paper; Github	https://github.com/jiawei-zhong/WAT_depots
Code for Spatial neighborhood ENrichment analySis and Evaluation (SENSE) framework	This paper; Github	https://github.com/jiawei-zhong/SENSE
ImageLab software v6.0.1	Bio-Rad	https://www.bio-rad.com/en-se/product/image-lab-software?ID=KRE6P5E8Z
GraphPad Prism v10.1.2	GraphPad	https://www.graphpad.com/
R v4.1.3	R Foundation	https://cran.r-project.org/bin/windows/base/
RStudio	Posit	https://posit.co/products/open-source/rstudio/
CellRanger v6.1.2 and v7.1.0	10X Genomics	https://www.10xgenomics.com/support/software/cell-ranger/
SoupX v1.6.2	Young et al.[50]	https://github.com/constantAmateur/SoupX
DoubletFinder v2.0.3	McGinnis et al.[51]	https://github.com/chris-mcginnis-ucsf/DoubletFinder
Space Ranger v2.0.0	10X Genomics	https://www.10xgenomics.com/support/software/space-ranger/latest
Cutadapt v4.1	Martin[52]	https://cutadapt.readthedocs.io/en/stable/
Loupe Browser v5.0.0	10X Genomics	https://www.10xgenomics.com/support/software/loupe-browser/latest
SpotClean v1.0.1	Ni et al.[8]	https://github.com/zijianni/SpotClean
scVI v0.16.2	Lopez et al.[10]	https://github.com/scverse/scvi-tools
Seurat v4.3.0 andv5.3.0	Hao et al.[53]	https://satijalab.org/seurat/
DemuxEM	Gaublomme et al.[54]	https://github.com/lilab-bcb/demuxEM
CellBender v0.2.0	Fleming et al.[55]	https://github.com/broadinstitute/CellBender
scds v1.14.0	Bais and Kostka[56]	https://github.com/kostkalab/scds
scDblFinder v1.12.0	Germain et al.[57]	https://github.com/plger/scDblFinder
Harmony v0.1.0	Korsunsky et al.[9]	https://github.com/immunogenomics/harmony?tab=readme-ov-file
Cell2location v0.1	Kleshchevnikov et al.[7]	https://github.com/BayraktarLab/cell2location
CellRank2 v2.0.6	Weiler et al.[24]	https://github.com/theislab/cellrank
CellChat v2.1.2	Jin et al.[24]	https://github.com/jinworks/CellChat
Bisque v1.0.5	Jew et al.[58]	https://github.com/cran/BisqueRNA
Fiji v2.17.0	Github	https://github.com/fiji/fiji
STAR v2.7.2a	Dobin et al.[59]	https://github.com/alexdobin/STAR
HTseq v2.0.3	Anders et al.[60]	https://github.com/htseq/htseq
Gencode v43	Mudge et al.[61]	https://www.gencodegenes.org/
ClusterProfiler v4.6.2	Yu et al.[62]	https://bioconductor.org/packages/release/bioc/html/clusterProfiler.html
DESeq2 v1.48.2	Love et al.[63]	https://bioconductor.org/packages/release/bioc/html/DESeq2.html

EXPERIMENTAL MODEL AND STUDY PARTICIPANT DETAILS

Adipose tissue samples were obtained within clinical studies approved by the regional institutional review boards in accordance with the Declaration of Helsinki. Samples used for the snRNA-seq, STx, and immunofluorescence imaging have been approved by the local ethics committee at the University of Leipzig (Reg. #017-12-23012012), and samples used for SAA and LPS protein stimulation

were approved in Stockholm (Clinical Trial identifier NCT01727245). All subjects provided written informed consent. In Leipzig, adipose tissue samples were collected from eight subjects undergoing bariatric surgery. Subcutaneous adipose tissue was obtained from the incision site of the first trocar in the left paramedian mid-abdomen. Omental samples were taken from the midsection of the pars libera of the greater omentum. Mesenteric samples were collected from the mesentery around the mid-jejunum, while mesocolic samples were obtained from the mesenteric region of the transverse colon. Additionally, epiploic samples were taken from the appendices epiploicae of the transverse colon. Clinical parameters for the included participants are listed in Table S1. In Stockholm, three subjects (all women, aged 30-51 years, with a BMI of 34.5-37.4) underwent bariatric surgery, and adipose tissue samples were collected from the abdominal subcutaneous area. The validation cohort data collection and processing were performed in accordance with the University of Pittsburgh Medical Center (UPMC) and Beth Israel Deaconess Medical Center institutional review boards. Paired subcutaneous, omental, and epiploic samples were obtained from four individuals undergoing either Roux-en-Y or vertical sleeve gastrectomy surgeries at UPMC. In total, two women and two men were included. Their clinical characteristics were the following (range, min-max): age (21-57 years), BMI (36.5-60.3 kg/m^2), HOMA-IR (7.0-17.8), and HbA1c (5.5-6.8 %).

METHOD DETAILS

Spatial transcriptomics using Visium spatial gene expression

Adipose tissue samples (n=36) were embedded in OCT (Tissue-Tek, Sakura Finetek) and sectioned into 16 μm thick sections using a CryoStar NX70 cryostat (Thermo Fisher Scientific). Blade temperature: -35°C; specimen temperature: -40°C. The sections were subsequently placed on Visium spatial gene expression slides, stored overnight at -80°C and processed according to the Visium Spatial Gene Expression protocol (10x Genomics). The resulting slide was incubated for 45 seconds at 37°C, before proceeding with an extended fixation with cold methanol (VWR Chemicals) at -20°C for 40 minutes. The slide was then gently dipped in 1x PBS to remove the OCT surrounding the tissue sections. Haematoxylin and eosin (H&E) staining was carried out by incubating the tissue sections for 3 min in Mayer's haematoxylin (Agilent Technologies), followed by 30 seconds in eosin (Sigma-Aldrich) (1:20 dilution in Tris buffer, pH 6) and mounted using 80% diluted glycerol. Bright-field images were acquired using the Metafer Slide Scanning platform and stitched in VSlide software (both from Metasystems). Permeabilization was carried out for 15 min as previously described.[12] Dual-indexed libraries of the tissue sections were generated following the Visium Library Preparation protocol. Libraries were sequenced on a NextSeq 2000 platform (Illumina) using P3 and P2 reagent and flow cell kits, with 1% PhiX spike-ins. The read lengths were 28 nt for R1 (spatial barcode and UMI), 10 nt for i7, 10 nt for i5, and 90 nt for R2 (insert).

Preprocessing of spatial transcriptomic data

We first used *Cutadapt* v4.1[52] to remove template switch oligos and polyA homopolymers. Manual image alignment and tissue-covered spots selection were performed in *Loupe Browser* v5.0.0. Because the biopsies were small, sections often varied in shape, and regions with folds, tears, or poor signal quality were excluded. Next, the processed data was demultiplexed and aligned to the genome by using *Space Ranger* v2.0.0. The hg38 human genome (refdata-gex-GRCh38-2020-A) from 10X Genomics was used. We leveraged *SpotClean* v1.0.1[8] to reduce lateral diffusion events. Spots with more than 40% of mitochondrial genes or 10% of hemoglobin genes were discarded.

Spatial data integration and cell type identification

SCTransform from *Seurat* v4.3.0[53] was used for normalization, standardization and identification of highly variable features. Independent components were calculated and used as input for *Harmony* v0.1.0[9] to correct for batch effects across donors and depots. The latent embedding of *Harmony* was adopted for spot clustering and dimension reduction. By leveraging latent embedding of *Harmony*, we built a shared nearest neighbor graph, clustered spots and visualized them in a two-dimensional embedding by using *FindNeighbors*, *FindClusters* and *RunUMAP*. Highly expressed genes of each cluster were calculated by *FindMarker*. We annotated each cluster by comparing their highly expressed genes with a previously published human adipose tissue STx dataset.[12]

Generation of single-nucleus RNA sequencing data

After the STx experiments, the OCT-embedded samples were processed for nuclei isolation after carefully removing the OCT surrounding the tissue. A total of 50-100 mg of tissue was placed into a gentleMACS C-tube containing 3 mL of freshly prepared nuclei isolation lysis buffer (5 mM CaCl, 3 mM, 3 mM MgAc, 2 mM EDTA, 0.5 mM EGTA, 10 mM Tris pH 8.0, 5 mM DTT, protease and RNAse inhibitors). The samples (n=34) were homogenized using a gentleMACS dissociator and incubated at 4°C for 5 min with an additional 3 mL of lysis buffer plus 0.4% Triton-X. The homogenate solution was transferred to a 50 mL conical tube over a 70 μm cell strainer and centrifuged at 1000 x *g* for 5 min at 4°C with a low break speed. The pellet was resuspended with 1 mL of 2% BSA-PBS and filtered through a 40 μm FlowMi strainer (SP SCIENCEWARE; Belart). The fluorescent dye Draq7 (Thermo Fisher Scientific) was added to each nuclei suspension sample for cell sorting using a FACS Melody system (BD Bioscience). Nuclei were sorted in DNA Lo-Bind tubes (Eppendorf AG) precoated with 500 μL of 2% BSA-PBS. The sorted nuclei were further centrifuged at 1000 x *g* for 5 min at 4°C. The pellet was resuspended with 50 μL of 2% BSA-PBS. Approximately 1000-1500 nuclei/μl were dispensed on the Chromium Next GEM Chip G according to the manufacturer's protocol (Chromium Next GEM Single Cell 3' Reagent Kits v3.1) and loaded into the 10x Chromium controller (10x Genomics). cDNA samples and snRNA-seq libraries were generated following the 10X Genomics protocol (Chromium Next GEM Single Cell 3' Reagent Kits v3.1). cDNA samples and snRNA-seq libraries quality and integrity were assessed using a DNA High Sensitivity

Bioanalyzer Chip (Agilent 2100 Bioanalyzer) and quantified using the Qubit dsDNA High Sensitivity assay kit (Thermo Fisher Scientific) following the manufacturers' instructions. Libraries were pooled and sequenced on NovaSeq 6000 S4 flow cell (Illumina) to a depth of approximately 360 million reads per library with 2 × 150 bp paired-end.

Preprocessing of snRNA-seq data

Cutadapt[52] was applied to remove adaptors. Trimmed sequencing data were processed using *Cell Ranger* v7.1.0 based on the default parameters to align to hg38 genome, demultiplex cell barcodes and generate cell-by-gene expression matrices. Next, we applied *SoupX* v1.6.2[50] and *DoubletFinder* v2.0.3[51] to remove ambient RNA contamination and doublets, respectively. Cells with more than 5% of mitochondrial RNA were filtered. Hemoglobin and mitochondrial genes, ribosomal protein families, *MTRNR* and *MALAT1* were excluded prior to performing downstream analyses.

snRNA-seq data integration and cell type identification

snRNA-seq matrices were integrated to remove batch effect across donors and depots using *scVI* v0.16.2.[10] Specifically, we used *Seurat* to merge all matrices and identify the top 2,000 highly variable features. The latent embedding was then generated by *get_latent_representation* from *scVI*. We adopted this for latent embedding cell clustering and dimension reduction. Highly expressed genes of each cell cluster were determined by *FindMarker*. We annotated clusters through comparison of highly expressed genes with well-established adipose tissue cell type specific markers.[13] The annotation was made hierarchical. The first level included broad cell classes (e.g., vascular, immune), while the second level of annotation contained specific cell types within each class.

Data generation and processing of the validation cohort

White adipose tissue snRNA-seq was performed as previously described.[64] Briefly, for each 10x run, 12 adipose samples were separately homogenized in TST buffer using a gentleMACS Dissociator (Miltenyi Biotec). Lysate was filtered through 40 μm and 20 μm nylon filters (CellTreat), centrifuging and resuspending in fresh buffer each time. After the second wash, each sample was incubated with NucBlue (Thermofisher scientific) as well as an individual hashtag antibody (BioLegend) for 45 min. After incubation, nuclei were washed and flow-sorted together into RT Reagent B (10x Genomics) using a Beckman Coulter MoFlo Astrios EQ with a 70 μm nozzle to remove poor quality nuclei and count the same number of nuclei per sample. After sorting, samples were immediately loaded on the 10x Chromium controller (10x Genomics) according to the manufacturer's protocol. Single Cell 3' v3.1 chemistry was used to process all samples, and cDNA and gene expression libraries were generated according to the manufacturer's instructions (10x Genomics). Gene expression libraries were multiplexed and sequenced on the Nextseq 500 (Illumina). Raw sequencing reads were processed into digital expression matrices using *Cell Ranger* v6.1.2 using GENCODE annotation GRCh38. *DemuxEM* v0.1.6[54] was used to sort cells into individual samples based on their antibody hashtags. Ambient RNA was removed from the processed DGEs using *CellBender* v0.2.0,[55] and doublet scores were calculated using both *scDblFinder* v1.12.0[57] and *scds* v1.14.0.[56] Cells were removed as doublets if they were both determined to be a doublet using *scDblFinder* and if they had a scds hybrid score > 1.5. Cells with < 800 UMIs were removed from the dataset, as were cells with > 10% of mitochondrial reads. We integrated the matrices using *scVI* and annotated each cluster as described above.

Spatial deconvolution

We performed *cell2location* v0.1[19] for the deconvolution of STx by using snRNA-seq data with the second level annotation (described above) as input. Default parameter settings were used for deconvolution analysis. Subsequently, cell type proportions for each spot were calculated by dividing the abundance of each cell type by the total abundance of a given spot.

Quantifying spatial neighborhood enrichment with *SENSE*

We developed Spatial neighborhood ENrichment analySis and Evaluation (*SENSE*) framework to measure spatial relationships between cell types. *SENSE* integrates deconvolution-derived cell-type proportions with neighborhood information to evaluate two complementary metrics: homotypic score (self-clustering preference) and heterotypic score (preferential co-occurrence between identities). *SENSE* is available via GitHub (https://github.com/jiawei-zhong/SENSE).

Homotypic score calculation

We extended the algorithm described in the previous study[12] by integrating it with the deconvolution results. Briefly, we let $X_{s,c}$ be the deconvolution-inferred proportion of cell type c in spot s. For each spot, $N(s)$ was defined as its six adjacent spots. The observed homotypic score $k_{obs}(s,c)$ was then calculated as:

$$k_{obs}(s,c) = X_{s,c} \times \sum_{j \in N(s)} X_{j,c}.$$

To estimate an expected (random) score, we permuted the coordinates within each slide 50 times. The expected score was then defined as the average over these permutations:

$$k_{exp}(s,c) = \frac{1}{50} \sum_{p=1}^{50} k_{obs}^{(p)}(s,c),$$

where p was defined as each permutation. The final homotypic score was obtained by normalizing the difference between the observed and expected scores by the total proportion of the cell type in the slide:

$$k(s,c) = \frac{k_{obs}(s,c) - k_{exp}(s,c)}{\sum_{s \in S} X_{s,c}},$$

where S was the set of all spots.

Heterotypic score calculation

We further extended our scoring approach to quantify co-occurrence between different cell types. The observed heterotypic score for cell types c and c' in spot s was computed as:

$$k_{obs}(s,c,c') = X_{s,c} \times X_{s,c'} + \frac{1}{4}\left(X_{s,c}\sum_{j \in N(s)} X_{j,c'} + X_{s,c'}\sum_{j \in N(s)} X_{j,c}\right).$$

We also permuted the coordinates 50 times to calculate the expected score and its standard deviation:

$$k_{exp}(s,c,c') = \frac{1}{50}\sum_{p=1}^{50} k_{obs}^{(p)}(s,c,c');$$

$$\sigma_{exp}(s,c,c') = \sqrt{\frac{1}{50-1}\sum_{p=1}^{50}\left(k_{obs}^{(p)}(s,c,c') - k_{exp}(s,c,c')\right)^2}.$$

The final z-score heterotypic score was determined as:

$$k(s,c,c') = \frac{k_{obs}(s,c,c') - k_{exp}(s,c,c')}{\sigma_{exp}(s,c,c')}.$$

Pseudo-time analysis

CellRank2 v2.0.6[24] was used for pseudo-time analyses, where asm00, 02, 03, and 08 were used as input. Diffusion pseudotime was employed by selecting the extremum of diffusion components as the root cell. The transition matrix was generated based on *CellRank2*'s *PseudotimeKernel* and visualized as streamlines in the UMAP embedding.

Cell-cell communication analysis

Cell-cell communication analysis was performed using *CellChat* v2.1.2[25] based on the curated ligand-receptor interaction database (*CellChatDB*). In brief, normalized gene expression matrices with level 1 annotation from different depots were provided as input to *CellChat*, respectively. The matrices were generated by combining snRNA-seq data (excluding adipocytes) with adipocyte information from STx. Donor identity was used as the batch variable.

Bulk deconvolution

Deconvolution of bulk proteomics data of human adipocyte differentiation was performed using a marker-based approach from *Bisque* v1.0.5.[58] The marker genes were calculated within the ASPC cluster.

IHC staining and imaging

WAT biopsies were embedded in paraffin blocks and subsequently cut into 7 μm thick sections, which were baked at 62°C for 45 min. After deparaffinization and serial dehydration steps, antigen retrieval was performed by heating the tissue sections in 10 mM citrate buffer pH 6.0 (tri-sodium citrate in distilled water) for 20 min using a microwave. Slides were washed three times with PBS containing 0.3% Triton X-100. Then, slides were blocked with protein block (Agilent Technologies, X090930-2) for 30 min at room temperature prior to primary antibody incubation. Primary antibody (anti-CES1 [1:500, 16912-1-AP, Proteintech], anti-KRT19 [1:200, ab52625, Abcam] and anti-CD68 [1:100, ab199000, Abcam]) was diluted in protein block (X090930-2, Agilent Technologies) and incubated on the sections overnight at 4°C. After three wash steps with washing buffer (0.05% Tween-20 [P1379, Sigma-Aldrich] in PBS), the slides were incubated with secondary antibodies (donkey anti-rabbit conjugated with Alexa Fluor 647 [1:200, A-31573, Thermo Fisher Scientific], donkey anti-rabbit conjugated with Alexa Fluor 555 [1:500, A-31572, Thermo Fisher Scientific], and donkey anti-mouse conjugated with Alexa Fluor 488 [1:500, A-21202, Thermo Fisher Scientific]) diluted in 0.1% Tween in PBS or protein block for an hour at room temperature. The slides were washed three times for 10 min with washing buffer. TrueView autofluorescence quenching kit (VEC-SP-8400-15, Vector labs) was applied following the manufacturer's instructions. Fluorescein-labeled lectin (1:200, FL-1041, Vector labs) or Dylight649-labeled lectin (1:200, DL-1048-1, Vector labs), together with Hoechst33342 (1:2000, ab228551, Abcam), was applied on the slides for 20 minutes. Lastly, the slides were washed once with PBS and swirled in MilliQwater before mounting on a #1.5 coverslip in VectaMount AQ Mounting Medium (H-5501, Vector labs).

Images were acquired on a Nikon Ti2 microscope equipped with a spinning disk confocal (Crest Optics V3), and a Kinetix sCMOS camera (Photometrics, 6.5um pixels). The imaging wavelengths used were for Fluorescein labelled lectin ex477 nm, em515/30, for Alexa Fluor 647 labeled CES1 ex637nm em685/40. Z-stack images (2.5 μm step size (Nyquist sampling) were acquired using a Nikon 10x/0.45 air objective. All data were acquired without saturation.

For the CD68-CES1 double stain, the images were acquired in the same way as above by using lasers ex405 nm and emission filter em438/24 for Hoechst, ex477 nm, and em515/30 for CD68, ex546, and em593/40 for CES1, and ex638 nm and em685/40 for lectin. Z-stack images (5 steps, á 0.9 μm) were acquired using a 20x objective, and 4x4 images were stitched together by using 15% overlap blending.

Quantification of CES1 signal

Quantification of the CES1 signal was performed in Fiji v2.17.0. More specifically, ten randomly selected regions were manually drawn based on lectin staining. The mean fluorescent intensity of CES1 in these regions was then measured after background subtraction from three randomly selected areas inside three adipocytes.

Human adipose tissue-derived stromal cell differentiation and stimulation

$CD55^+$ ASPCs were cultured, and adipogenic differentiation was induced as previously described.[65] Briefly, cells were obtained from subcutaneous WAT of one anonymous male donor and maintained at 37°C in a humidified incubator with 5% CO_2 in proliferation medium (DMEM [31885-023 Gibco], 10 mM HEPES [15630-056 Gibco], 10% fetal bovine serum [FBS, SV30160, Hyclone], 50 μg/mL Penicillin-Streptomycin [15140-122 Gibco] supplemented with 2.5 ng/mL fibroblast growth factor 2 [FGF2, F0291, Sigma-Aldrich]). Three days after the cultures reached confluence, FGF2 was withdrawn from the medium, and differentiation was initiated the following day using a medium based on 1:1 (v:v) DMEM and Ham's F12 (21765-037, Gibco), supplemented with 5 μg/mL insulin (I9278, Sigma-Aldrich), 1 μM dexamethasone (D1756, Sigma-Aldrich), 100 μM 3-isobutyl-1-methylxanthine (IBMX, I5879, Sigma-Aldrich), 0.2 nM 3,3',5-Triiodo-L-thyronine (T6397, Sigma-Aldrich), 10 μg/mL transferrin (T8158, Sigma-Aldrich) and 10 μM rosiglitazone (71740, Cayman Chemicals) for 3 days. After this, dexamethasone and IBMX were removed. Rosiglitazone was removed after 10 days and the cells were used before or 12 days after inducing adipogenic differentiation (proliferating hADSC and adipocyte in Figures 6 and S6, respectively). To study the effects of LPS, cells were incubated with 1, 10, or 100 ng/mL LPS derived from e. coli (O55:B5, L4524, Sigma-Aldrich) with 1% FBS for 24 hours or with 10 ng/mL LPS and 1% FBS for 0, 0.5, 2, 4, 8 and 24 hours. Similarly, cytokines were added for 24 hours with 1% FBS present and compared to control cells receiving sterile distilled water and 1% FBS. TNF-α (H8916, Sigma-Aldrich) was used at a concentration of 2.5 ng/mL, and IL-6 (200-06, Thermo Fisher Scientific) and IL-1β (H6291, Sigma-Aldrich) at a concentration of 10 ng/mL. For studying pathways responsible for *SAA1/SAA2* mRNA induction, inhibitors and blocking antibodies (anti-TLR4 [1:100, 14-9917-82, eBioscience], anti-CD14 [1:50, 14-0149-82, eBioscience], Z-VAD-FMK [20 μM, FMK001, Bio-Techne], BAY-11-7082 [2.5 μM, 196870, Sigma-Aldrich], STAT3i VII [0.5 μM, 573103, Sigma-Aldrich]) were added 1 hour prior to addition of 1% FBS and 10 ng/mL LPS for 24 hours. 0.5% (v/v) DMSO (D2650, Sigma-Aldrich) was used as a control.

Adipose tissue-derived endothelial cell isolation and culture

Endothelial cells from human WAT were isolated as described previously.[66] Briefly, adipose tissue was minced and enzymatically digested for 30 min at 37°C in supplemented KnockOut DMEM (10829018, Thermo Fisher Scientific) containing penicillin/streptomycin (15140122), Antibiotic-Antimycotic (15240062), 1 mM sodium pyruvate (11360070), 1× MEM non-essential amino acids (11140050), 2 mM L-glutamine (25030024), 1× Endothelial Cell Growth Factor supplements (ECGS/heparin; C-30120, PromoCell), collagenase I (17100017), 0.25 U/mL Dispase, and 7.5 mg/mL DNase I. Following digestion, the cell suspension was passed through a 100 μm cell strainer (Falcon, Corning 352360) and washed in PBS containing 0.5% BSA and 2 mM EDTA. Endothelial cells were enriched by sequential magnetic depletion of $CD45^+$ cells and positive selection of $CD31^+$ cells using MicroBeads (130-045-801 and 130-091-935, Miltenyi) and columns according to the manufacturer's instructions. Isolated cells were cultured on 0.1% gelatin–coated plates in supplemented Endothelial Cell Growth Medium 2 (C-22011, PromoCell) at 37°C and 5% CO_2. Single-donor cultures were used between passages 3–4. To assess LPS responsiveness, cells were treated with 1, 10, or 100 ng/mL LPS (L4524, Sigma-Aldrich), sterile distilled water (vehicle), and 860 nM insulin (I9278, Sigma-Aldrich) for 24 h.

THP1 cell culture

Human monocytic THP1 cells were cultured in RPMI 1640 GlutaMAX medium (61870044, Gibco) supplemented with 10 mM HEPES (15630-056, Gibco), 50 U/mL penicillin and 50 μg/mL streptomycin (15140-122, Gibco) and 10% FBS (SV30160, Hyclone) that was heat-inactivated for 30 min at 56°C. Cells were maintained in a humidified chamber with 5% CO_2 at 37°C. To differentiate THP-1 monocytes into M0 macrophages, cells were seeded at a density of 2×10^5 cells/well in a 24-well plate and treated with 30 ng/mL phorbol-12-myristat-13-acetat (PMA, P8139, Sigma-Aldrich) dissolved in dimethyl sulfoxide (DMSO, D2650, Sigma-Aldrich) for 48 hours. The medium containing PMA was then removed, and the cells were incubated in fresh medium with 1, 10, and 100 ng/mL LPS (O55:B5, L4524, Sigma-Aldrich) or sterile distilled water for 24 hours.

Magnetic bead separation and LPS stimulation of $CD45^+$ cells

Previously isolated SVF samples were separated into two fractions with CD45 microbeads according to the manufacturer's instructions (130-045-801, Miltenyi). The cells were directly harvested for RNA isolation (74004, Qiagen), and a small fraction of $CD45^+$ cells

was separated into maintenance media for a 24-hour stimulation with 100 ng/mL LPS (L4524, Sigma-Aldrich) or sterile distilled water as a control.

Gene expression analysis by quantitative reverse transcription PCR

A column-based RNA isolation kit (740902.50, Macherey-Nagel) was used to isolate RNA from cells. RNA concentration was measured with a microdrop-plate (N12391, Thermo Fisher Scientific) in a Varioskan microplate reader (Thermo Fisher Scientific). RNA was reverse transcribed using iScript cDNA synthesis kit (1708891, Bio-Rad). Synthesized cDNA was diluted to a concentration of 1 ng/μl and analyzed by quantitative polymerase chain reaction using SYBR chemistry (1708882, Bio-Rad). Each experiment was performed in technical triplicate, and two housekeeping genes, *18S* and *B2M*, were used to normalize the results for the cell line data, whereas *RPLP0* was used for normalization of the isolated primary cells. Expression levels were calculated using the Livak method (delta-delta Ct method).[67] Primer sequences used were as follows:

SAA1 fw: AACTATGATGCTGCCAAAAGG, rev: TGGATATTCTCTCTGGCATCG,
SAA2 fw: CTGCAGAAGTGATCAGCA, rev: ATTATATGCCATATCTCAGC,
IL6 fw: CCTGAACCTTCCAAAGATGGC, rev: TTCACCAGGCAAGTGTCCTCA,
CCL2 fw: AGAATCACCAGCAGCAAGTGTCC, rev: TCCTGAACCCACTTCTGCTTGG,
CXCL8 fw:CACTGCGCCAACACAGAAAT, rev:TTCTCAGCCCTCTTCAAAAACTTC,
PLIN1 fw: TGGAGACTGAGGAGAACAAG, rev: ATGTCACAGCCGAGATGG,
LEP fw: CTGTGCGGATTCTTGTGGCT, rev: GAGGAGACTGACTGCGTGTGT,
18S fw: TGACTCAACACGGGAAACC, rev: TCGCTCCACCAACTAAGAAC,
B2M fw: AAGGACTGGTCTTTCTATCTC, rev: GATCCCACTTAACTATCTTGG,
RPLP0 fw: AACTCTGCATTCTCGCTTCC, rev: GGACTCGTTTGTACCCGTTG.

Western blot

Proteins were isolated from cell cultures by lysing PBS-washed cells with RIPA buffer (89901, Thermo Fischer Scientific) complemented with protease and phosphatase inhibitors (11836170001 and 4906837001, respectively, Sigma-Aldrich) on ice. The lysate was scraped and centrifuged at 14,000 rpm for 20 min at +4°C in microcentrifuge tubes. Protein concentration was determined by using a bicinchoninic acid assay (BCA, 23235, Thermo Fisher Scientific). Proteins were reduced and denatured in Laemmli buffer (1610747, Bio-Rad) supplemented with β-mercaptoethanol (M3148, Sigma-Aldrich), and boiled at 95°C for 5-10 min. In total, 10-15 μg of denatured protein was loaded on 12% SDS-PAGE gels (5671045, Bio-Rad) together with a protein size marker (1610373, Bio-Rad). In blots where the proteins of interest were the same size, lysates were subdivided into equal amounts and loaded on two gels. The electrophoresis was performed at 90 V for approximately 1 hour, and the proteins were transferred onto PVDF membranes using a semi-wet transfer system (TransBlot Turbo, 1704274, Bio-Rad). The membranes were blocked for 1 hour at room temperature with a 3% blocking reagent (B501-0500, Rockland Immunochemicals) or 5% BSA (A9647, Sigma-Aldrich) in Tris-buffered Saline Tween-20 (TBS-T). Primary antibodies (anti-NFκB p65 [8242, Cell Signaling], anti-phospho-NFκB p65 [Ser536] [3033, Cell Signaling], anti-STAT3 [9139, Cell Signaling], anti-phospho-STAT3 [Tyr705] [9145, Cell Signaling], and anti-α-tubulin [2125, Cell Signaling]) were diluted 1:1000 in the blocking buffer and incubated at +4°C overnight before washing 3x10 min with TBS-T. Secondary antibodies (anti-rabbit-HRP [7074, Cell Signaling] and anti-mouse-HRP [W4021, Promega]) were diluted 1:10,000 in blocking buffer, and incubations were carried out for 1 hour at room temperature. The membranes were washed three times in TBS-T for 10 min, and chemiluminescence was detected with ECL Select reagent (RPN2235, Cytiva) using the CFX imaging system (Bio-Rad). Protein quantification was carried out from three individual experiments using the ImageLab software 6.0.1 (Bio-Rad), and the results were normalized to the loading control.

SAA quantification in conditioned media

Cell culture supernatants were collected following 72-hour incubation in the presence or absence of 10 ng/mL LPS, spun at 10,000 x *g* for 5 min at 4 °C. Human SAA was measured with an ELISA kit (ab100635, Abcam) according to the manufacturer's instructions.

Stromal-vascular fraction isolation for LPS and recombinant SAA treatment

The SVF from subcutaneous adipose tissue biopsies obtained from individuals undergoing bariatric surgery was isolated after collagenase digestion as described previously.[68] Red blood cells were removed by incubating the cells in 1X RBC lysis buffer (00-4333-57, eBioscience) for 5 min and washing the cells in maintenance media (DMEM low glucose [31885-023, Gibco] supplemented with 2% FBS [SV30160, Hyclone], 50 IU/mL penicillin and 50 μg/mL streptomycin [15140122, Gibco]). The freshly isolated cells were incubated in maintenance media with 10 μg/mL human recombinant SAA1 (TP310664, OriGene) per 100,000 cells or with an equal volume of vehicle (25 mM Tris-HCl, 100 mM glycine, pH 7.3, 10% glycerol) The recombinant protein was produced in eukaryotic cells and confirmed not to contain endotoxins (<0.3 EU/mL measured in both treatment and vehicle solutions, data not shown). For LPS stimulation, the cells were incubated with 1 ng/mL LPS (L4524, Sigma-Aldrich) or with an equal volume of sterile distilled water. After 6 hours at 37°C and 5% CO_2, the cells were harvested, and total RNA was isolated with a column-based isolation method (74004, Qiagen). The mRNA was sequenced at NovoGene with NovaSeq X Plus Series (PE150) to an average sequencing depth of 20 million reads.

Bulk RNA-seq data analysis of LPS and recombinant SAA treated samples

We mapped the raw sequencing reads to the hg38 genome using *STAR* v2.7.2a.[59] The number of reads per gene was counted using *HTseq* v2.0.3[60] and *Gencode* v43.[61] Differential expression analysis was performed via *DESeq2* v1.34.0.[63] Low count reads (< 10) were removed, and *DESeq2* was used with the multi-factor design for conditions and subjects, and log2 fold changes were shrunk using the normal mean posterior distribution. Normalized counts were transformed using the variance stabilizing transformation method from *DESeq2* to facilitate clustering analysis. Gene ontology enrichment analysis was performed using *clusterProfiler*.[62] *Seurat*[53] was used to assess gene module scores in snRNA-seq data. A gene signature corresponding to the differentially expressed genes (DEGs, log2 fold change >1, adjusted $P<0.05$) from RNA-seq was applied to the snRNA-seq data using the *AddModuleScore* function.

Gene set enrichment analysis

All genes ordered by log fold change were input into the *gseKEGG* function from *clusterProfiler* v4.6.2.[62] Pathways were considered significant if their false discovery rate-adjusted *P value* was less than 0.05.

QUANTIFICATION AND STATISTICAL ANALYSIS

Statistics were performed in *R* v4.1.3 or GraphPad Prism v10.1.2. Differences in cell type proportions among depots were computed by fitting a linear mixed-effects model with age, sex, and BMI as fixed covariates and donor as a random effect. Significance was determined via likelihood ratio tests. Protein quantification results are reported as the mean ± standard error of the mean (SEM) with individual data points shown from three independent experiments, or six individual subjects, as indicated in the figure legends. mRNA quantification results are reported as the geometric mean ± 95% confidence intervals with individual data points presented from each independent experiment. Student's t test or one-way ANOVA with normality assumption and Dunnett's or Bonferroni's multiple testing correction was used to determine the significance of the gene and protein quantification data; the test used is indicated in each figure legend.